

Intermediate Field Directions Recorded in Pliocene Basalts in Styria (Austria): Evidence for Cryptochron C2r.2r-1

Elisabeth Schnepf (✉ elisabeth.schnepf@unileoben.ac.at)

Montanuniversitat Leoben <https://orcid.org/0000-0002-1685-9974>

Patrick Arneitz

ZAMG: Zentralanstalt für Meteorologie und Geodynamik

Morgan Ganerød

NGU: Norges geologiske undersøkelse

Robert Scholger

Montanuniversität Leoben

Ingomar Fritz

Joanneum University of Applied Sciences: FH Joanneum GmbH

Ramon Egli

ZAMG: Zentralanstalt für Meteorologie und Geodynamik

Roman Leonhardt

ZAMG: Zentralanstalt für Meteorologie und Geodynamik

Full paper

Keywords: Paleomagnetism, paleointensity, transitional field configuration, cryptochron C2r.2r-1, ³⁹Ar/⁴⁰Ar dating, Styria (Austria), volcanic rocks

Posted Date: April 13th, 2021

DOI: <https://doi.org/10.21203/rs.3.rs-408695/v1>

License: © ⓘ This work is licensed under a Creative Commons Attribution 4.0 International License.

[Read Full License](#)

1 **Title: Intermediate Field Directions Recorded in Pliocene Basalts in Styria**
2 **(Austria): Evidence for cryptochron C2r.2r-1**
3
4 *for EPS* “full paper”
5
6 **Author #1: Elisabeth Schnepf, Palaeomagnetic Laboratory Gams, Chair of**
7 **Applied Geophysics, Montanuniversität Leoben, Gams 45, A8130 Frohnleiten,**
8 **Austria, elisabeth.schnepf@unileoben.ac.at**
9 Author #2: Patrick Arneitz, Conrad Observatorium, ZAMG - Zentralanstalt für
10 Meteorologie und Geodynamik, Hohe Warte 38, 1190 Vienna, Austria,
11 patrick.arneitz@zamg.ac.at,
12 Author #3: Morgan Ganerød, Geological Survey of Norway, P.O. Box 6315 Torgarden,
13 NO-7491 Trondheim, Norway, Morgan.Ganerod@NGU.NO
14 Author #4: Robert Scholger, Palaeomagnetic Laboratory Gams, Austria,
15 robert.scholger@unileoben.ac.at
16 Author #5: Ingomar Fritz, Universalmuseum Joanneum, Studienzentrum Naturkunde,

17 Weinzöttlstraße 16, 8045 Graz, Austria, ingomar.fritzqmuseum-joanneum.at

18 Author #6: Ramon Egli, ZAMG, Vienna, Austria, ramon.egli@zamg.ac.at

19 Author #7: Roman Leonhardt, ZAMG, Vienna, Austria, roman.leonhardt@zamg.ac.at

20 **Corresponding author**

21

22 **Abstract**

23 Pliocene volcanic rocks from South-East-Austria were paleomagnetically investigated.
24 Samples were taken from 28 sites located on eight different volcanoes. Rock magnetic
25 investigations revealed that magnetic carriers are Ti-rich or Ti-poor titanomagnetites
26 with mainly pseudo-single-domain grain size. Characteristic remanent magnetization
27 directions were obtained from alternating field as well as from thermal demagnetization.
28 Four localities give reversed directions agreeing with the expected direction from
29 secular variation. Another four localities of the Klöch-Königsberg volcanic complex (3)
30 and the Neuhaus volcano (1) have reversed directions with shallow inclinations and
31 declinations of about 240° while the locality Steinberg yields a positive inclination of
32 about 30° and 200° declination. These aberrant directions cannot be explained by local
33 or regional tectonic movements. All virtual geomagnetic pole positions are located on
34 the southern hemisphere. Four virtual geomagnetic poles lie close to the geographic
35 pole, while all others are concentrated in a narrow longitude sector offshore South
36 America (310° to 355°) with low virtual geomagnetic pole latitudes ranging from -15°
37 to -70° . The hypothesis that a transitional geomagnetic field configuration was recorded

38 during the short volcanic activity of these five localities is supported by 9 paleointensity
39 results and $^{39}\text{Ar}/^{40}\text{Ar}$ dating. Virtual geomagnetic dipole moments range from 1.1 to
40 $2.9 \cdot 10^{22} \text{ Am}^2$ for sites with low VGP latitudes about 60° and from 3.0 to $9.3 \cdot 10^{22} \text{ Am}^2$
41 for sites with higher virtual geomagnetic pole latitudes. The new $^{39}\text{Ar}/^{40}\text{Ar}$ ages of 2.51
42 $\pm 0.27 \text{ Ma}$ for Klöch and $2.39 \pm 0.03 \text{ Ma}$ for Steinberg allow for the correlation of the
43 Styrian transitional directions with cryptochron C2r.2r-1 of the geomagnetic polarity
44 time scale.

45

46 **Keywords**

47 Paleomagnetism, paleointensity, transitional field configuration, cryptochron C2r.2r-1,
48 $^{39}\text{Ar}/^{40}\text{Ar}$ dating, Styria (Austria), volcanic rocks

49

50 **Introduction**

51 The Earth's magnetic field is generated in the outer core by an interacting system of
52 liquid and electrical currents, which form the so-called geodynamo. For our
53 understanding of the geodynamo knowledge of the temporal change of the geomagnetic

54 field is crucial. Direct observations cover only a few hundred years (e.g., Arneitz et al.,
55 2017). Paleomagnetic records obtained from rocks provide information on the
56 geological past (e.g., Gubbins and Herrero-Bervera, 2007). Volcanic rocks give spot
57 readings of the geomagnetic field and eventually provide a temporal succession if
58 stratigraphy is known. In addition to the stable field configuration and its secular
59 variation, documenting transitional field configurations during reversals or excursions
60 are of high interest in order to constrain geodynamo mechanisms and support modelling
61 of the geomagnetic field evolution during such critical events (e.g., Leonhardt et al.
62 2009).

63 The geomagnetic polarity time scale (GPTS, e.g., Gradstein et al., 2012) is continually
64 refined (Ogg et al. 2016). It is based on long sedimentary series obtained from ocean
65 drilling and on records from lavas which are precisely correlated by astrochronology
66 and radiometric dating (e.g., Channell et al., 2009; Singer, 2014). The last 5 Ma of the
67 GPTS is divided into chrons and subchrons by more than 20 polarity transitions. Further
68 instabilities, called cryptochrons or excursions, such as short living or aborted reversals,
69 are documented (e.g., Singer, 2014).

70 Here, we present a re-investigation of sites from the Styrian volcanic field in south-east
71 Austria for which paleomagnetic directions have been published some decades ago
72 (Pohl and Soffel, 1982; Mauritsch, 1972; Table 1). While the Miocene sites showed
73 normal directions in agreement with secular variation, the Pliocene sites (Bojar et al.,
74 2013) yielded mainly inverse directions which do not lie within the range expected from
75 secular variation. These anomalous directions observed in Styria potentially recorded
76 excursions or transitional states of the geomagnetic field. In order to test this
77 hypothesis, most sites have been resampled and new sites have been added. Here, full
78 vector paleomagnetic data obtained with state-of-the-art demagnetisation and
79 paleointensity techniques are provided for the Pliocene volcanoes. New $^{39}\text{Ar}/^{40}\text{Ar}$ dating
80 of two sites with transitional directions improved previous K-Ar age constraints of
81 Bojar et al. (2013) and support a correlation with the geomagnetic polarity time scale.

82

83  Table 1

84

85 **Geological setting and field work**

86 The sampling area is located at the south-eastern margin of the Alps in the Styrian Basin
87 (Fig. 1, Gross et al. 2007). It is part of the Pannonian Basin and separated from other
88 subbasins by the South Burgenland Swell in the south-east. The north-eastern boundary
89 is built by a Penninic unit, while in the north, west and southwest the Styrian Basin is
90 encircled by crystalline Austroalpine units and the Graz Paleozoic, which forms the
91 basement as well. The formation of the Styrian Basin started in the Late Oligocene to
92 Miocene at the final collision stage of the Adriatic and European plates and is connected
93 to the alpidic lateral extrusion and subduction-related extension in the Pannonian region
94 (e.g., Neubauer and Genser 1990). The sedimentary filling of the basin started in the
95 Early Miocene and the major tectonic events were accompanied by volcanism
96 producing volcanoclastics and high-K effusive rocks (Ebner and Sachsenhofer 1991).
97 The second volcanic phase, starting in the Upper Miocene (Bojar et al. 2013), is
98 dominated by a large number of tuff occurrences with phreatomagmatic origin (Pöschl
99 1991, Fritz 1996) and continued up to the Pliocene/Early Pleistocene with effusive

100 alkaline rocks and volcanoclastic tuffs (Balogh et al. 1994). A total of 30-40 eruption
101 centers have been identified (Kollmann 1965). The different volcanoclastic rocks prove
102 the former presence of maars, scoria cones, lava lakes and lava flows. Today, exposed
103 volcanic remnants (e.g., lava flows, diatremes) form prominent highs in the landscape
104 (Gross et al. 2007). K-Ar ages and petrological description are available for six Pliocene
105 lavas (see Table 1, Seghedi et al. 2004; Balogh et al. 1994).

106 Paleomagnetic sampling was carried out in several campaigns using an electrically or
107 gasoline powered drill with diamond bit. The cores were orientated with a magnetic
108 compass and whenever possible, with a sun compass. Azimuth differences between
109 magnetic and sun compass readings were always $<5^\circ$. Samples were taken from 28 sites
110 distributed over 8 volcanic units (see Table 1 and Fig. 1). Two of the volcanic edifices
111 have been sampled extensively: the Klöch-Königsberg complex, with samples taken in
112 and around the big quarry of Klöch (KN01 to KN13) and at Zaraberg (KN14, KN15),
113 and 3 dikes outcropping on the Königsberg tuff cone (Tieschen: TS, TD). Additionally,
114 the synvolcanic lake sediment deposited on the top of the lavas in Klöch quarry was
115 sampled with plastic boxes (Table 1). Another five sites were distributed over the big

116 quarry Steinberg south of Mühldorf (SB01 to SB05). Directional results from six of our
117 sites had already been published by Pohl and Soffel (1982) and were resampled at the
118 same places or nearby.

119

120 **Rock and paleomagnetic laboratory procedures**

121 Thermomagnetic bulk susceptibility curves of crushed material, $\kappa(T)$, were measured in
122 air using a MFK1-FA susceptibility meter (Agico) with a CS-3 temperature control unit.

123 For a better understanding of the development of thermal alteration, the effects of
124 thermal cycling with starting temperatures between 150–290°C and increments of
125 100°C were also investigated. Continuous thermal demagnetisation was performed for a
126 few mini-specimens drilled along the characteristic remanent magnetisation direction in
127 order to check for evidence of self-reversal magnetizations. Hysteresis and isothermal
128 remanent magnetization (IRM) backfield curves were measured on mini-cores (4–5
129 mm) with a Micromag Model 3900 vibration sample magnetometer (VSM).

130 Characteristic remanent magnetizations obtained with stepwise alternating field (AF) as
131 well as thermal demagnetization (except site KN10) have been measured with a

132 cryogenic (2G) or a spinner (Agico JR6) magnetometer. AF demagnetization was
133 performed in line with the magnetometer or with external devices (MI AFD 300,
134 Magnon International, or ASC D-2000) while a MMTD60 or a MMTDSC furnace
135 (Magnetic measurements) was used for thermal demagnetization. AF demagnetization
136 was performed in 10 to 18 steps up to a maximum field of 140 to 300 mT depending on
137 the behavior of the specimen and the equipment. Thermal demagnetization was based
138 on 10 to 13 steps between 100 and 600°C with increments of 20, 40 or 50°C. The
139 experiment was stopped when the residual magnetization was lower than 5% of the
140 initial natural remanent magnetization (NRM) or an increase of magnetization was
141 observed above 400°C.

142 Selection of well-suited specimens for paleointensity determination was difficult
143 because rock magnetic experiments often revealed the presence of magnetic carriers
144 with low thermal stability. Furthermore, viscous overprints, which hamper
145 paleointensity determination have been detected in many samples. In addition to
146 thermal stability of $\kappa(T)$ -cycling and lack of viscous overprints, specimens for
147 paleointensity determination were selected according to the absence or weakness of

148 secondary components and remanence stability during thermal demagnetization.

149 Temperature steps were adjusted to the expected unblocking temperatures and the onset

150 of thermal alteration. Paleointensity experiments were conducted on 70 specimens (18

151 standard inch specimens and 52 mini-specimens of 9 mm diameter drilled from the inch

152 specimens) from 14 sites (Table 1). Thirteen sites were not tested because they failed

153 the selection criteria given above. The Thellier technique modified by Coe (1967) using

154 the protocol MT4 of Leonhardt et al. (2004) was applied. Thirteen to 15 heating steps

155 starting at 90°C or 200°C, depending on the expected blocking temperature range, have

156 been used. Temperature increments were comprised between 20 and 50°C and the

157 maximum temperature was 500 °C, 550°C or ~600°C. A laboratory field between 15

158 and 40 μ T adjusted to the expected intensity was applied. Six or 7 pTRM-checks, 5 or 6

159 tail checks (Riisager & Riisager 2001) and 3 to 5 additivity checks (Krása et al. 2003)

160 were included. Heating was performed in a MMTD24 furnace (Magnetic

161 measurements) using the rapid cooling rate setting, magnetization was measured with

162 an AGICO JR-6A Dual Spinner Magnetometer and susceptibility was checked with a

163 Bartington MS2B/MS3 Magnetic Susceptibility Meter ASC D-2000 after each

164 temperature step. Because chemical alteration sometimes started before the secondary
165 component was removed, Thellier experiments were combined with AF
166 demagnetization for 42 specimens (Marshall et al. 1988) by applying a 15 mT AF
167 demagnetization prior to each magnetization measurement (Table S1, additional files).
168 All paleointensity measurements were carried out at the Conrad Observatory (ZAMG).

169

170 **Isotopic dating**

171 Specimens from 4 of our sites were selected for $^{39}\text{Ar}/^{40}\text{Ar}$ -dating, but inspection of thin
172 sections revealed that only 2 sites provided material suited for dating.

173 The samples were crushed and sieved to obtain 180 – 250 μm fractions. The finer
174 particles were decanted in tap water and the coarser residue ultrasonically washed in
175 acetone and deionized water several times. The optically best suited grains, void of any
176 coatings, were handpicked under a stereomicroscope. The samples were packed in
177 aluminum capsules together with the Taylor Creek Rhyolite (TCR) flux monitor
178 standard along with zero age reagent grade K_2SO_4 and optical grade CaF_2 salts for
179 interference corrections. The samples were irradiated at the MTA reactor (Hungary) for

180 ~ 2 hours, with a nominal fast neutron flux density of c. $5.5 \times 10^{13} \text{ n} \cdot \text{cm}^{-2} \cdot \text{s}^{-1}$. The
181 interference correction factors for the production of isotopes from Ca and K are reported
182 in the additional files, Table S2. The groundmass grains were placed in a 3.5 mm pit
183 size aluminum sample disk and step heated using a defocused 3.5 mm CO₂ laser beam
184 from Photon Machine Fusions 10.6 with a flat energy spectrum. The gases extracted
185 from the sample cell were expanded into a Piston Free Stirling Cryocooler for trapping
186 potential water vapor, and further expanded into a two-stage low volume extraction line
187 (~ 300 cm³). Both stages were equipped with SAES GP-50 (st101 alloy) getters, the
188 first running hot (c. 350 °C) and the second running at room temperature. The samples
189 were analyzed with an MAP 215–50 mass spectrometer in static mode, installed at the
190 Geological Survey of Norway. The peaks and baseline (AMU = 36.2) were determined
191 during peak hopping for 15 cycles (15 integrations per cycle, 30 integrations on mass
192 ³⁶Ar) on the different masses (^{40–36}Ar) on a MasCom electron multiplier (MC217) in
193 analogue mode and linearly regressed back to zero inlet time. Blanks were analyzed
194 every third measurement. After blank correction, a correction for mass fractionation,
195 ³⁷Ar and ³⁹Ar decay and neutron-induced interference reactions produced in the reactor

196 was performed using in-house software AgeMonster, written by M. Ganerød. This
197 software implements the equations of McDougall and Harrison (1999) and the newly
198 proposed decay constant for ^{40}K after Renne et al. (2010). A $^{40}\text{Ar}/^{36}\text{Ar}$ ratio of $298.56 \pm$
199 0.31 from Lee et al. (2006) was used for the atmospheric argon correction and mass
200 discrimination calculation using a power law distribution of the masses. Finally, we
201 calculated J-values relative to an age of 28.619 ± 0.036 Ma for the TCR fluence monitor
202 (Renne et al., 2010).

203

204 **Results**

205 *Rock magnetism*

206 The thermomagnetic behaviour of susceptibility was measured for at least one sample
207 per site. It was studied more intensively for the sites selected for paleointensity
208 determination using also thermal cycling runs. The investigated samples yielded a broad
209 spectrum of $\kappa(T)$ -curves. These curves can be roughly divided into five types (Fig. 2).
210 Type A has a single, high Curie point (T_c) between 512 and 598°C and can be almost
211 completely reversible, which points to presence of magnetite as the dominant magnetic

212 carrier. Irreversible curves are more common, with a susceptibility decrease to about
213 half of the initial value (e.g., Fig. S1, appendix: KN15-6). Thermal cycling shows that
214 alteration starts above 450–500°C. In some cases, also a second Curie point may occur
215 at a higher temperature, pointing to the presence of some maghemite or hematite (e.g.,
216 Fig. S1, KN12-7, SK0202B). Type A was found in only five localities (KN, TS/TD, SB,
217 SK and WA, see also Fig. S1, appendix and Table S3, additional files).

218 The overwhelming majority of the sites showed a much less stable thermomagnetic
219 behavior (Type B). It is characterized by the presence of a low Curie point, presumable
220 carried by Ti-rich titanomagnetite, which transforms to magnetite when heated above
221 600°C. Curves can be almost reversible also at higher temperatures (e.g., Fig. S1,
222 KN06-2), but normally the formation of new magnetite is indicated by a bump present
223 below 500°C resulting in a new Curie temperature around 580°C (Fig. 2 and e.g., Fig.
224 S1 KN04-5, KN08-5, NH0202I, SB0106I, SB0301, SB0507I, ST0209I). Thermal
225 cycling shows that the onset of alteration starts already around 300°C. Heating to lower
226 temperatures often yielded T_c values of 120–350°C. Type B samples are thus
227 characterized by a highly variable Ti-content. Thermal alteration often prevented a

228 proper estimation of T_c . Thellier experiments of type B specimens were performed from
229 90 to 360°C in 30°C-steps, because thermal cycling often revealed good reversibility up
230 to 400 °C. Nevertheless, the presence of viscous overprints led to the failure of Thellier
231 experiments for all tested type B specimens.

232 Type C shows a steady decrease of susceptibility with a high Curie point between 544–
233 581°C and some reversible curves were obtained. In the other cases, alteration is
234 relatively weak, starts mostly around 500°C (e.g., Fig. S1, KN14-10), and is visible
235 mainly in the low (<400°C) temperature range. The susceptibility is relatively low and
236 paramagnetic behavior is observed. This type is only present in one sample of SB02
237 (Fig. S1) and site KN14, a tuff baked by the overlying lava flow KN15.

238 Type D shows three bumps both in heating and cooling curves, which may represent
239 three magnetic carriers associated with Ti-rich and Ti-poor Magnetite and/or
240 Maghemite. A proper T_c determination is possible only for the third decay and yields to
241 values above 600°C. Such curves were only found in two sites: AM03 und TS03 (cf.
242 Fig. S1).

243 Finally, type E shows a mixture of two or three minerals and strong alteration. A high

244 Curie point at ~580°C indicates the formation of magnetite, while all other phases
245 disappear. Stability against thermal cycling is low and alteration starts at about 300°C.
246 Sites NH02 and ST02 were dominated by this behavior (cf. Fig. S1).
247 Samples with $\kappa(T)$ -types B and E were not used for palaeointensity experiments, except
248 for sites where better material was not available (cf. Table S3).
249 Hysteresis parameters were measured with a VSM for two to seven samples per site.
250 The Day-diagram (Fig. 3, Table S4, additional files) indicates that most samples plot in
251 the lower part of the pseudo-single domain range close to the three mixing curves of SD
252 and MD magnetite grains of Dunlop (2002).
253
254 *Paleomagnetic directions*
255 Directions are well constrained for only 8 sites (see Fig. S2, appendix), while weak to
256 significant secondary overprints are present at 20 sites. Demagnetization experiments
257 were done with AF (181 specimens) and thermally (142 specimens) and processed with
258 the Remasoft3.0 software in order to obtain the characteristic remanent magnetization
259 (ChRM) directions from principal component analysis (PCA, Kirschvink 1980).

260 Fig. 4(a) shows an almost ideal demagnetization behavior for site Altenmarkt without
261 secondary components and a very good agreement between AF and thermal data. Site
262 Stein (Fig. 4 b) features only weak, easily removable secondary components and the
263 ChRM directions are very well clustered (Fig. S2). Sites Stradner Kogel (Fig. 4 c) and
264 Waltra (Fig. 4 d) feature mostly clustered NRM directions and nearly antiparallel
265 overprints, most likely originating from of the present geomagnetic field. Specimens
266 with NRM directions far from the ChRM cluster have strong overprints which were
267 removed with 5 to 30 mT AF demagnetization (e.g., Fig. 4 c-d).

268 Five sites were sampled at Steinberg volcano within a big quarry. With the exception of
269 two specimens, 5–30 mT or 75–200°C were needed to remove secondary components
270 (Fig. 5). Comparisons of these treatments with the median destructive field (MDF) and
271 median destructive temperature (MDT) reveal that a large part of the magnetization was
272 affected by secondary components (Fig. 6, left). Scattered directions were often
273 obtained during thermal demagnetization (Fig. 5 b-d) along with chemical alteration, as
274 suggested by a magnetization increase around 300°C (e.g., Fig. 5 a). Some specimens
275 (13%) were completely unstable and did not yield any ChRM. Valid ChRM directions

276 are similar for all sites but show a considerable dispersion (Table 1, Fig. S2, SB01 to
277 SB05).

278 Directions of the Klöch quarry and at Zaraberg sites are often affected by some scatter,
279 with well-clustered ChRM directions being observed only in 2 cases (KN08, and KN15).

280 Strong overprints were encountered in most of the demagnetization experiments. AF
281 demagnetization with 5 to 30 mT was sufficient to remove these secondary components,
282 while elevated temperatures up to 380°C were needed thermal demagnetization. Here
283 MDT and MDF values (Fig. 6, right) are generally higher than for Steinberg and some
284 of the Klöch-sites have a good thermal stability with MDT values above 400°C. The
285 origin of the secondary components was tested by great circle analysis with examples
286 plotted in Fig. 7. They show that the demagnetization path leads to the present field
287 direction. Accordingly, these overprints are viscous magnetizations caused by the
288 present geomagnetic field. This was often but not always the case. Fig. 8 (a, b) shows
289 demagnetization examples from Klöch for those sites which had only weak secondary
290 components. The overprints are approximately antiparallel with an increase of intensity
291 at the beginning of demagnetization, followed by straight lines with consistent

292 directions. All sites from Klöch and Zaraberg have ChRM directions with relatively low
293 negative inclinations and declinations between 210° to 230° (Fig. S2). The samples
294 from the synvolcanic lake sediment layer (Table 1, KN10) showed well defined
295 clustered directions after removal of the viscous overprint, which are similar to those of
296 the volcanic sites (Fig. S2). Similar directions were also observed for the lavas from
297 Neuhaus and for three dikes in Königsberg north of the Klöch volcano (Fig. S2, NH02
298 and TD01, TD02 TS03/TD04). The examples show moderate secondary overprints (Fig.
299 8 c, d) and well-defined ChRM directions. Considerable directional scatter among
300 samples is observed for all sites with these unusual directions (see Fig. S2).

301

302 *Paleointensities*

303 Evaluation of the paleointensity experiments started with determination of the ChRM
304 direction, which failed for 11 specimens (Table S1). A trend towards the laboratory
305 field direction was also often observed. The ThellierTool4.22 software (Leonhardt et al.
306 2004) with default parameters for Classes A and B was used for preliminary evaluation
307 and the results were checked carefully and sometimes adjusted, for instance by

308 removing initial heating steps when they were obviously affected by an overprint. A
309 few specimens, slightly exceeding class B criteria but providing a good straight line fit,
310 were also accepted (Class C). Another 27 specimens failed to give acceptable results.
311 For further characterization of our 37 results, additional parameters were calculated,
312 such as the NRM fraction FRAC, the Arai plot curvature $|\vec{k}|$, and the correlation
313 coefficient R_{corr}^2 (Table S1, for definitions see Paterson et al. 2014, 2015). These
314 parameters were checked with the software of Béguin et al. (2020). Three sets of criteria
315 are used for the final classification (Table 2): the strict (S) criteria were based on the
316 MC-CRIT.B1 set of Paterson et al. (2015). The same parameters are used for the
317 moderate (M) criteria based on the modified TTB set of Paterson et al. (2014). The third
318 set takes the rather weak (W) criteria of Bono et al. (2019).

319

320 **Table 2:** Criteria sets were used for classification of the paleointensity results.

Criterion	Strict (S)	Moderate (M)	Weak (W)	range
n	≥ 5	≥ 5	≥ 5	5 – 15
FRAC	≥ 0.45	≥ 0.30	–	0.19 – 0.97
β	≤ 0.1	≤ 0.1	–	0.01– 0.15
q	≥ 5	≥ 3	–	1.6 – 52.7
$ \vec{k} $	≤ 0.13	≤ 0.48	–	0.00 – 1.01
MAD_{Anc}	≤ 6	≤ 10	≤ 10	1.1 – 5.8
α	≤ 10	≤ 15	–	0.6 – 14.3
DRAT	–	–	≤ 10	1.5 – 11.0
δCK	≤ 7	≤ 9	–	1.2 – 6.8
δpal	≤ 9	≤ 18	–	0 – 40.8
δTR	≤ 3.4	≤ 20	–	1.4 – 13
Δt^*	≤ 9.0	≤ 50	–	0 – 7.3
R_{corr}^2	–	–	≥ 0.9	0.915 – 1.000
Reference	Paterson et al. (2015)	Modified from Paterson et al. (2014)	Bono et al. (2019)	

321 n : number of data points used for the linear fit; FRAC: NRM fraction; β : standard deviation of
 322 slope; q : quality factor (Coe et al., 1978); $|\vec{k}|$: Arai plot curvature; MAD_{Anc} : maximum angular
 323 deviation of anchored line; α : angular difference between anchored and not-anchored solution;
 324 DRAT: deviations of pTRM checks; δCK : pTRM checks; δpal : cumulative check difference; δTR :
 325 relative intensity difference of tail checks; Δt^* : normalized tail of pTRM; R_{corr}^2 : correlation
 326 coefficient of fit line (for definitions see Paterson et al. 2014 and references therein). The last
 327 column gives the range of the values obtained for the successful experiments.

328

329 Representative examples for each set of criteria and one failed experiment are given in

330 Fig. 9. Only 3 specimens fulfill the strict criteria (Fig. 9 a), with very good linearity of

331 the Arai-plot and in the orthogonal vector plot of demagnetization, positive pTRM,

332 additivity and tail checks and a very small error of the obtained paleointensity (Table
333 S1). Moderate criteria were fulfilled by 24 specimens. About half of them have also a
334 good Arai plot linearity, but they do fail one to three of the S criteria, which are often
335 δpal or δTR and sometimes $|\vec{k}'|$ or FRAC. The other specimens fulfilling M criteria
336 show concave Arai curves with an increase of TRM capacity and a trend towards the
337 laboratory field direction, and in one case a decrease of TRM capacity followed by an
338 increase (Fig. 9 b and c). In these cases, slightly curved Arai plots were accepted over
339 ranges where the alteration was still very low, as indicated by matching pTRM and
340 additivity checks. Accordingly, the main parameters responsible for S criteria failures
341 were $|\vec{k}'|$ and in a few cases FRAC, δTR , δpal or q. Ten specimens that met only the
342 weak criteria are not particularly different in their behavior (Fig. 9 d and e) but they do
343 fail for $|\vec{k}'|$ or FRAC and often they bear a considerable secondary component (Fig. S3
344 d). Some specimens failed because of a strong TRM capacity decrease above 400°C,
345 which was followed by an increase due to the formation of new minerals (Fig. 9 f).

346

347 $^{39}\text{Ar}/^{40}\text{Ar}$ -dating

348 Ar release spectra from incremental heating were obtained for 10 samples from 2

349 volcanic localities. Spectrum analysis criteria used to determine the sample ages include

350 at least 3 overlapping consecutive steps (95% confidence), accounting for >50%

351 cumulative ^{39}Ar release. An inverse isochron age was then calculated from these release

352 steps and we use those results as sample ages. We chose this strategy since the isochron

353 method does not contain any assumption regarding the trapped atmospheric

354 contaminant.

355 The gas release spectra with inverse isochrons are displayed in Table 3 and Fig. S4. The

356 release spectra of all samples from Klöch contain a plateau. Inverse isochron results

357 yield an inverse weighted mean age of 2.51 ± 0.27 Ma (MSWD: 0.46, P: 0.71). Only 3

358 samples from Steinberg met the aforementioned age criteria (SB0202A, SB0403A and

359 SB404A) with an inverse weighted mean age of 2.46 ± 0.12 (MSWD: 0.72, P: 0.49).

360

361  Table 3

362

363 **Discussion**

364 *Mean paleomagnetic directions and virtual geomagnetic poles*

365 Most specimens showed weak to strong secondary overprints. In almost all cases, an
366 increase of the intensity at the beginning of the demagnetization experiments suggests
367 that the secondary component has an approximately antiparallel direction. Because all
368 sites have ChRM directions nearly opposite to the present-day field, secondary
369 components are most likely viscous overprints. This is supported by the fact that, for
370 many specimens, great circles fitted to the secondary component run through the present
371 field direction. The magnetization increase with respect to the NRM was considerable,
372 often exceeded 30% of the initial NRM intensity. Accordingly, specimens with a pure
373 primary TRM, which is a prerequisite for paleointensity determination, were rare.
374 Secondary components were mostly removed with ≤ 30 mT AF demagnetization, while
375 300°C or even more were required during thermal demagnetization. Nevertheless, well
376 defined ChRM directions have been obtained from 164 AF and 111 thermal
377 demagnetization experiments. Moreover, paleointensity experiments (see below)

378 provided further 49 ChRM directions from the oriented specimens and mini-cores. The
379 site mean directions were calculated hierarchically, averaging specimens of
380 independently oriented samples first, and then sites using Fisher (1953) statistics. In
381 most cases well defined mean ChRM directions were obtained (Table 1) with values of
382 the precision parameter k (Fisher 1953) ranging from 11 to 1276, and α_{95} values
383 between 2° and 15° . The mean ChRM directions of only 4 sites are reversed and within
384 the range of secular variation (Fig. 10). The remaining sites show anomalous directions
385 confined to the from $190\text{--}240^\circ$ declination sector. Sixteen sites have low negative
386 inclinations and 5 sites have low positive inclinations. The confidence circles are
387 generally larger for sites with intermediate directions. Nevertheless, magnetic cleaning
388 was successful and provided well defined reliable mean ChRM directions.

389 Calculation of the virtual geomagnetic poles (VGP, Table 1 and Fig. 11) shows that all
390 sites have reversed polarities and only 4 sites cluster close to the geographic pole having
391 high VGP latitudes ($< -70^\circ$ see Table 1, cluster A in Fig. 11). Furthermore, VGPs are
392 mainly confined in a narrow longitudinal sector from 290 to 360°E . Two more clusters
393 with low VGP latitudes can be identified, one (cluster B) below -30° and another

394 (cluster C) at about -45° . Other sites from Klöch and Zaraberg investigated by Pohl &
395 Soffel (1982) fall also in this cluster and the poles of Pohl & Soffel (1982) are well
396 reproduced (Table 1 and Fig. 11). This VGP distribution obviously does not represent
397 secular variation. Accordingly, the possibility of tectonic movements must be taken into
398 consideration. In this case, the recorded anomalous directions would require a $\sim 30^\circ$
399 rotation of the Klöch-Königsberg and Neuhaus volcanoes and an even larger rotation
400 for Steinberg. The lavas of two volcanoes are well exposed in large quarries and there is
401 no geological evidence for local displacements or regional movements affecting all 5
402 localities with unusual directions. Sites with directions in the range of SV and those
403 with anomalous directions are distributed all over the volcanic field and no correlation
404 with tectonic features is found (Fig. 12). For instance, Klöch and Königsberg are
405 separated by a normal fault, but the paleomagnetic directions are very similar.
406 Furthermore, the synvolcanic lake sediment layer (Table 1, KN10) yielded a ChRM
407 direction within the cluster of the Klöch-Königsberg lavas. The detritus came very
408 likely from volcanic ejection of the Königsberg, which implies also a stratigraphic
409 constraint between the Klöch and Königsberg lavas. The sediment is layered nearly

410 horizontally, displays the visible underlying morphology and does not give evidence for
411 local tectonic movements. Furthermore, the similar directions of Klöch-Königsberg
412 complex and Neuhaus volcano would require the same local tectonic movement to
413 explain their unusual but very similar directions, which is rather unlikely. Finally, the
414 Miocene Gleichenberg volcano (in blue in Fig. 12) recorded normal polarity directions
415 in the range of secular variation (Pohl and Soffel, 1982). Accordingly, a large-scale
416 tectonic rotation after the Miocene can be excluded for the area.
417 Therefore, the only remaining conclusion is that the Styrian volcanoes recorded
418 intermediate field directions. This hypothesis was further tested by investigation of the
419 paleointensity.

420

421 *Paleointensity*

422 Paleointensity determination was difficult, due to secondary components and chemical
423 alteration during heating. Thellier experiments were performed for 15 sites and the
424 failure rate was about 50%. Only 3 specimens fulfill the strict MC-CRIT.B1 criteria set
425 of Paterson et al. (2015), while for the moderate criteria set, the NRM fraction FRAC

426 was lowered to 0.3, considerably less than recommended by Paterson et al. (2014; 2015:
427 0.45). FRAC (see Shaar and Tauxe, 2013) was introduced instead of the fraction factor f
428 (Coe et al. 1978) because f may be overestimated in case of strongly concave Arai plots.
429 This behavior is caused by the presence of a large amounts of MD particles, but also by
430 strong viscous overprints. Viscous overprints have been often observed during our
431 paleointensity experiments, for instance for the specimen shown in Fig. 9 d, which lost
432 about one third of the NRM during the first heating step in combination with AF
433 demagnetization. This loss was accompanied by a strong directional change. $\kappa(T)$ (Fig.
434 S1) gives no indication for the presence of a mineral with low Curie temperature. While
435 the secondary component is still present until 350°C, very little TRM is gained in the
436 Thellier experiment. The viscous component was relatively large compared to the
437 paleo-TRM because this TRM was acquired in a much weaker field than the
438 present-day value. The fraction factor f is >0.5 for this example (Table S1) and,
439 although somewhat overestimated, f appears to be more appropriated than FRAC in
440 such cases. The hysteresis parameters of this specimen point also to a large MD fraction,
441 which explains the strong curvature $|\vec{K}|$ in the Arai plot. Mineral alteration starts at

442 ~500°C (Fig. S1), as shown by the last pTRM check. Accordingly, the selected data
443 points give a reasonable paleointensity estimate and this is also the case for the example
444 in Fig. 9 e. It is obvious that most of our samples do not have magnetic properties which
445 are suited to provide very precise paleointensities. Instead, the aim of the study is rather
446 to find support for the intermediate character of the directions by intensity
447 measurements and thus to have more indications for a transitional field configuration.
448 Hence, many of the results which we take into consideration allow only for a rough
449 assessment of paleointensity and do not fulfil the various published and widely accepted
450 more strict criteria (e.g., Kissel and Laj 2004; Biggin et al. 2007; Paterson et al. 2014;
451 2015; Cromwell et al. 2015; Tauxe et al. 2016). Although such reliability criteria sets
452 are undoubtedly useful for statistical investigation for long term trends of the field, a too
453 rigorous application rejects many experiments which could yield slightly uncertain, but
454 important information about the paleofield configuration.
455 Finally, paleointensity results from 10 sites are taken into consideration and 8 mean
456 paleointensity values have been calculated (Table 4), in one case by combining single
457 values for 2 sites from Steinberg volcano. These mean values are robust and remain

458 within their error margins when a stricter selection (only strict and moderate criteria
459 accepted) is made (Table S1).

460 Fig. 13 shows a summary of all accepted paleointensity results together with the site
461 means. A large variation of paleointensities is seen between the sites, while the
462 within-site dispersion is considerably smaller.

463 Data in Fig. 13 are grouped according to the above described VGP clusters. Class M
464 paleointensity results are present in all groups and the class W results do not show
465 larger deviations. Paleointensities of sites with low VGP latitudes lie in the range from
466 8 to 13 μT and only 5 μT has been determined for the lowest VGP latitudes. These
467 values are relatively low compared with the field intensity which was on average about
468 $35\pm 8 \mu\text{T}$ for the past 5 Ma (Muxworthy, 2017). While one site with high VGP latitude
469 has a relatively large intensity of 57 μT , the values from the Stradner Kogel sites are
470 only around 20 μT . Nevertheless, a rough correlation is seen between VGP latitude and
471 paleointensity or virtual geomagnetic dipole moment (VDM, see Table 4). This strongly
472 supports the hypothesis that the low latitude VGPs were recorded during a transitional
473 or excursions field configuration.

474

475 **Table 4** Paleointensity results of the Styrian lavas.

Location	Latitude (°N)	Longitu- de (°E)	Name	D (°)	I (°)	α_{95} (°)	Plat (°N)	PLong (°E)	PI (μ T)	sPI (μ T)	VDM (10^{22} Am ²)	sVDM (10^{22} Am ²)
Altenmarkt	47.005	15.912	AM03	187.6	-64.3	1.9	-84.7	293.7	57.4	3.4	9.3	1.1
Stradner Kogel	46.841	15.926	SK02	198.5	-57.6	2.3	-73.9	311.6	22.0		3.9	
Waltra	46.849	15.952	WA02	204.8	-60.6	3.3	-71.5	293.4	17.4	0.5	3.0	0.2
Klöch 12	46.767	15.968	KN12	211.6	-40.1	6.2	-55.2	318.3	12.0	2.0	2.6	0.8
Klöch 14	46.764	15.946	KN14	211.8	-28.8	5.7	-48.9	325.2	8.6	0.7	2.0	0.3
Klöch 15	46.764	15.946	KN15	219.2	-33.5	3.8	-47.1	314.1	12.9	4.2	2.9	1.9
Tieschen 01	46.783	15.954	TD01	214.4	-33.7	4.5	-50.1	319.4	11.2	2.5	2.6	1.1
Tieschen 03	46.787	15.956	TS03/TD04	207.9	-42.2	4.3	-58.4	321.4	10.5	3.9	2.2	1.6
Steinberg SB	46.935	15.917	SB01-05	200.7	28.8	4.7	-25.0	353.8	4.9	2.6	1.1	1.2

476 *D*: declination of the ChRM; *I*: inclination of the ChRM; α_{95} : 95% confidence circle radius of the
 477 Fisher (1953) statistics; Plat: latitude of the VGP position; Plon: longitude of the VGPe position;
 478 PI: mean paleointensity; sPI: standard deviation of paleointensity; VDM: virtual dipole moment
 479 from PI; sVDM: standard deviation of VDM.

480

481 *Ages and correlation with Geomagnetic Instability Time Scale*

482 K/Ar data obtained from lavas or associated tuffs of our sites give an age interval
 483 comprised between 2 and 4 Ma for the Pliocene effusive volcanoes in the Styrian basin
 484 (Bojar et al. 2013 and references therein, Table 1). New ³⁹Ar/⁴⁰Ar-dating performed on
 485 samples from 2 localities of our collection was successful for the Klöch and Steinberg

486 volcanoes, which carry transitional directions. They gave weighted locality mean ages
487 of 2.51 ± 0.27 Ma (Klöch) and 2.46 ± 0.12 Ma (Steinberg), respectively. The $^{39}\text{Ar}/^{40}\text{Ar}$
488 ages (Table 3) agree within their error margins and the age average of 2.47 ± 0.11 Ma
489 allows for correlation with the GPTS (Fig. 14). The transitional lavas are certainly
490 younger than the Gauss-Matuyama reversal and the most likely correspondence is the
491 cryptochron C2r.2r-1 (2.420 – 2.441 Ma, Cande and Kent 1992). According to Singer et
492 al. (2014; Laj and Channell 2007 and references therein), this is the lowermost
493 geomagnetic excursion in the Matuyama chron and is recorded in marine sediments as
494 well as in terrestrial lava flows on Ouhau, Hawaii (Hawala: ~ 2.51 Ma, Herrero-Bervera
495 et al. 2007; Wheeler Air Force core: ~ 2.46 Ma, Guillou et al. 2018) and on Santiago
496 Island, Cape Verde (2.411 Ma, Knudsen et al. 2009). Guillou et al. (2018) propose 2.46
497 ± 0.006 Ma as age of cryptochron C2r.2r-1. Channell et al. (2020) emphasize that
498 excursions have synchronous global manifestation in many cases. Accordingly, our
499 transitional directions provide further evidence of cryptochron C2r.2r-1.

500

501 *Distribution of VGPs*

502 The VGP positions of our group B lie in the South Atlantic, east of the Falklands, while
503 those of Steinberg (group C) are found east of St. Helena (Fig. 14). Hoffman (2000)
504 identified the South Atlantic and Central Asia as regions for preferred VGP-positions of
505 the Matuyama-Brunhes reversal for North Atlantic marine sediments. While different
506 recurrent pole positions west of Australia were found for Tahiti (Hoffman and Singer
507 2004) and further evidence for this preferred region is presented in a review (Hoffmann
508 et al. 2019) of Cenozoic palaeomagnetic transitional field records obtained from lavas in
509 the Southern Hemisphere (e.g., south Indian Ocean, eastern Australia and New Zealand),
510 a subordinate cluster of VGPs in the South Atlantic is present in these studies as well.
511 The situation is different when records from the northern hemisphere are considered
512 (Hoffmann and Singer 2004). Clusters of VGPs in the South Atlantic are found for
513 several transitional records spanning Miocene to Pleistocene ages. They were obtained
514 in the Mediterranean region (Tric et al. 1991; Valet and Laj 1984), the Atlantic Ocean
515 (Riisager et al. 2003, Leonhardt et al 2002) or in California (Glenn et al. 1999). Here the

516 Gauss-Matuyama reversal was recorded. Accordingly, VGP positions associated with
517 transitional field states have been detected in the South Atlantic. Aside from that, the
518 most prominent magnetic anomaly of the present geomagnetic field is situated in South
519 Atlantic and Engbers et al. (2020) provide evidence that anomalous long-term
520 geomagnetic field behavior of this region was already present ~10 Ma ago which can be
521 explained by core–mantle interaction.

522 Unlike to the two $^{39}\text{Ar}/^{40}\text{Ar}$ ages presented here, the K/Ar ages for the Pliocene Styrian
523 volcanic rocks span a much longer time interval. For instance, two K/Ar ages obtained
524 for Neuhaus volcano (VGP group B) differ from each other (Table 1). Only the younger
525 one overlaps with the new $^{39}\text{Ar}/^{40}\text{Ar}$ age of Klöch, but the intermediate directions
526 suggest that both volcanoes recorded one and the same short-living geomagnetic event.

527 Balogh et al. (1994) already suspected the Neuhaus ages to be overestimated because of
528 excess argon. This is strongly supported by our paleomagnetic and dating results.

529 Another K/Ar age is available for one dike from Königsberg (2.17 ± 0.13 Ma, Tieschen,
530 Seghedi et al. 2004, see Table 1). It is slightly younger but overlaps with the new age
531 for Klöch volcano within a two-sigma error (95% probability). Hence, all lavas of VGP

532 group B and C could have cooled down in a very short time interval. For the sites
533 Waltra and Stradner Kogel the low paleointensities (Fig 13) and the pole positions close
534 the VGP cluster B (Fig 14) suggest that Stradner Kogel volcano could have been
535 formed shortly before or after the geomagnetic excursion. Accordingly, at least 3 or 4 of
536 the Styrian volcanoes may have been formed in a short time interval corresponding to
537 the duration of a geomagnetic cryptochron. It remains difficult to assign the duration of
538 such an event. According to Cande and Kent (1992) the duration is less than 10 to 30
539 kyr. A recent investigation of the Laschamp excursion (Cooper et al. 2021) used ancient
540 New Zealand kauri trees for investigating atmospheric radiocarbon and revealed a
541 duration of only 1500 years.

542

543 **Conclusions**

544 Paleomagnetic directions from 27 sites from 6 volcanic centers and one volcanic
545 complex of the Styrian volcanic field have been obtained and confirm previous results
546 of Pohl and Soffel (1982). All VGPs have reversed polarity. Only 4 are in the range of
547 secular variation, while the others have low reversed VGP latitudes in the South

548 Atlantic. The anomalous directions cannot be explained by local or regional tectonics.
549 Low paleointensities and $^{39}\text{Ar}/^{40}\text{Ar}$ dating support that all intermediate directions were
550 recorded during an unstable field configuration. The Styrian basalts provide further
551 evidence for cryptochron C2r.2r-1 about 2.4 Ma ago.

552

553 **References**

- 554 Arneitz P, Leonhardt R, Schnepf E, Heilig B, Mayrhofer F, Kovacs P, Hejda P, Valach F, Vadasz G,
555 Hammerl C, Egli R, Fabian K, Kompein N (2017) The HISTMAG database: Combining
556 historical, archaeomagnetic and volcanic data. *Geophys. J. Int.* 210:1347–1359. doi:
557 10.1093/gji/ggx245.
- 558 Balogh K, Ebner F, Ravasz C (1994) K/Ar-Alter tertiärer Vulkanite der südöstlichen Steiermark und des
559 südlichen Burgenlandes. In: Lobitzer H, Csaszar G, Daurer A (eds) Jubiläumsschrift 20 Jahre
560 Geologische Zusammenarbeit Österreich-Ungarn. 2. Geologische Bundesanstalt, Wien, p 55
- 561 Béguin A, Paterson G, Biggin AJ, de Groot L (2020) Paleointensity.org: an online, open source,
562 application for the interpretation of paleointensity data. *Geochem Geophys Geosyst* 21
563 doi:10.1029/2019GC008791.
- 564 Biggin AJ, Perrin M, Dekkers MJ. (2007) A reliable absolute palaeointensity determination obtained
565 from a non-ideal recorder. *Earth Planet Sci Lett* 257:545-563. doi: 10.1016/j.epsl.2007.03.017.
- 566 Bojar H-P, Bojar A-V, Hałas S, Wójtowicz A (2013) K/Ar geochronology of igneous amphibole
567 phenocrysts in Miocene to Pliocene volcanoclastics, Styrian Basin, Austria. *Geological*
568 *Quarterly* 57:405-416. doi.org/10.7306/gq.1102.
- 569 Bono RK., Tarduno JA., Nimmo F, Cottrell RD. (2019) Young inner core inferred from Ediacaran
570 ultra-low geomagnetic field intensity. *Nature Geosci* 12:143-147. doi:
571 10.1038/s41561-018-0288-0.
- 572 Cande SC, Kent DV. (1995) A new Geomagnetic Polarity Time Scale for the late Cretaceous and
573 Cenozoic. *J Geophys Res* 97:13917-13951. doi: 10.1029/92JB01202.
- 574 Channell JET, Singer BS, Jicha BR (2020) Timing of Quaternary geomagnetic reversals and excursions
575 in volcanic and sedimentary archives. *Quaternary Science Reviews* 228:106114. doi:

- 576 10.1016/j.quascirev.2019.106114.
- 577 Channell JET, Xuan C, Hodell DA (2009) Stacking paleointensity and oxygen isotope data for the last 1.5
578 Myr (PISO-1500). *Earth Planet Sci Lett* 283:14-23. doi: 10.1016/j.epsl.2009.03.012.
- 579 Coe RS, Grommé SC, Mankinen EA (1978) Geomagnetic paleointensities from radiocarbon-dated lava
580 flows on Hawaii and the question of the Pacific nondipole low. *J Geophys Res* 83:1740-1756.
581 doi: 10.1029/JB083iB04p01740.
- 582 Coe RS (1967) Palaeo-intensity of the Earth's magnetic field determined from tertiary and quaternary
583 rocks. *J Geophys. Res.* 72:3247– 3262. doi: 10.1029/JZ072i012p03247.
- 584 Cooper A, Turney CS M., Palmer J, Hogg A, McGlone M, Wilmshurst J, Lorrey AM, Heaton TJ, Russell
585 JM, McCracken K, Anet JG, Rozanov E, Friedel M, Suter I, Peter T, Muscheler R, Adolphi F,
586 Dosseto A, Faith JT, Fenwick P, Fogwill CJ, Hughen K, Lipson M, Liu J, Nowaczyk N,
587 Rainsley E, Bronk Ramsey C, Sebastianelli P, Souilmi Y, Stevenson J, Thomas Z, Tobler R,
588 Zech R (2021) A global environmental crisis 42,000 years ago. *Science* 371:811-818. doi:
589 10.1126/science.abb8677.
- 590 Cromwell G, Tauxe L, Staudigel H, Ron H (2015) Paleointensity estimates from historic and modern
591 Hawaiian lava flows using glassy basalt as a primary source material. *Phys Earth Planet Int*
592 241:44-56. doi: 10.1016/j.pepi.2014.12.007.
- 593 Day R, Fuller M, Schmidt VA (1977) Hysteresis properties of titanomagnetites: Grain-size and
594 compositional dependence. *Phys Earth Planet Int* 13:260-267. doi:
595 10.1016/0031-9201(77)90108-X.
- 596 Dunlop D (2002) Theory and application of the Day plot (Mrs/Ms versus Hcr/Hc), 2, Application to data
597 for rocks, sediments and soils. *J Geophys Res* 107:EPM5-1-15. doi: 10.1029/2001JB000487.
- 598 Engbers YA, Biggin A, Bono RK (2020) Significantly high palaeomagnetic dispersion suggests
599 long-lived anomalous behavior in the South Atlantic. *Proc Natl Acad Sci* 117:18258-18263. doi:
600 10.1073/pnas.2001217117.
- 601 Flügel HW, Neubauer F (1984) Steiermark: Erläuterungen zur geologischen Karte der Steiermark,
602 1:200.000. Geologische Bundesanstalt.
- 603 Fisher RA (1953) Dispersion on a sphere. *Proc. R. Soc. London A*-127:295-305. doi:
604 10.1098/rspa.1953.0064.
- 605 Fritz I (1992) Geomagnetische Untersuchungen an Vulkaniten aus dem Bereich Altenmarkt bei
606 Riegerburg (Oststeirisches Neogenbecken). *Mitteilungen naturwissenschaftlicher Verein*
607 Steiermark 122:29-37.
- 608 Fritz I (1996) Notes on the Plio-/Pleistocene volcanism of the Styrian Basin. *Mitteilungen der*

609 Gesellschaft der Geologie- und Bergbaustudenten in Österreich 41:87-100.

610 Glen JMG, Coe RS, Liddicoat JC (1999) A detailed record of paleomagnetic field change from Searles
611 Lake, California: 2. The Gauss/Matuyama polarity reversal. *J Geophys Res* 104:12,883-12,894.
612 doi: 10.1029/1999JB900048.

613 Gradstein M, Ogg JG, Schmitz M, Ogg G (2012) *The Geologic Time Scale 2012*. Elsevier, Amsterdam.

614 Gross M, Fritz I, Piller WE, Soliman A, Harzhauser M, Hubmann B, Moser B, Scholger R, Suttner TJ,
615 Bojar H-P (2007) *The Neogene of the Styrian Basin, Guide to Excursions*. *Joannea Geol Paläont*
616 9:117-193.

617 Gubbins D, Herrero-Bervera E (2007) *Encyclopedia of geomagnetism and paleomagnetism*. Springer,
618 Dordrecht.

619 Guillou H, Scao V, Nomade S (2018) $^{40}\text{Ar}/^{39}\text{Ar}$ age of cryptochron C2r.2r-1 as recorded in a lava
620 sequence within the Ko'olau volcano (Hawaii, USA). *Quaternary Geochronology* 43:91-101.
621 doi: 10.1016/j.quageo.2017.10.005.

622 Herrero-Bervera E, Browne E, Valet JP., Singer BS, Jicha BR (2007) Cryptochron C2r.2r-1 recorded 2.51
623 Ma in the Koolau Volcano at Halawa, Oahu, Hawaii, USA: paleomagnetic and $^{40}\text{Ar}/^{39}\text{Ar}$
624 evidence. *Earth Planet Sci Lett* 254:256-271. doi: 10.1016/j.epsl.2006.11.023.

625 Hoffman KA, Camps P, Carlton M (2019) Rare palaeomagnetic evidence of long-term mantle control of
626 the geodynamo and possible role of the NAD field in the reversal process. *Geophys J Int*
627 221:142-150. doi: 10.1093/gji/ggz480.

628 Hoffman KA, Singer BS (2004) Regionally recurrent paleomagnetic transition fields and mantle
629 processes. In: Channell JET, Kent DV, Lowrie W, Meert JG (eds) *Timescales of the*
630 *Paleomagnetic Field*. AGU, Geophysical Monograph, Vol. 145. American Geophysical Union
631 doi:10.1029/145GM17.

632 Hoffman KA (2000) Temporal aspects of the last reversal of Earth's magnetic field. *Phi. Tran. R Soc*
633 *Lond A* 358:1181-1190. doi: 10.1098/rsta.2000.0580.

634 Kirschvink JL (1980) The least squares line and plane and the analysis of paleomagnetic data. *Geophys J*
635 *R astr Soc* 62:699-718. doi: 10.1111/j.1365-246X.1980.tb02601.x.

636 Kissel C, Laj C (2004) Improvements in procedure and paleointensity selection criteria (PICRIT-03) for
637 Thellier and Thellier determinations: application to Hawaiian basaltic long cores. *Phys Earth*
638 *Planet Int* 147:155-169. doi: 10.1016/j.pepi.2004.06.010.

639 Knudsen MF, Holm PM, Abrahamsen N (2009) Paleomagnetic results from a reconnaissance study of
640 Santiago (Cape Verde Islands): identification of cryptochron C2r.2r-1. *Phys Earth Planet Int*
641 173:279-289. doi: 10.1016/j.pepi.2009.01.009.

- 642 Laj C, Channell JET (2007) Geomagnetic excursions. *Treat Geophys* 5, 373-416. doi:
643 10.1016/B978-044452748-6.00095-X.
- 644 Lee JY, Marti K., Severinghaus JP, Kawamura K, Yoo HS, Lee JB, Kim JS (2006) A redetermination of
645 the isotopic abundances of atmospheric Ar. *Geochim Cosmochim Acta* 70:4507-4512. doi:
646 10.1016/j.gca.2006.06.1563.
- 647 Leonhardt R, McWilliams M, Heider F, Soffel HC (2009) The Gilsá excursion and the
648 Matuyama/Brunhes transition recorded in $^{40}\text{Ar}/^{39}\text{Ar}$ dated lavas from Lanai and Maui, Hawaiian
649 Islands. *Geophys J Int* 179:43-58. doi: 10.1111/j.1365-246X.2009.04264.x.
- 650 Leonhardt R, Heunemann C, Krása D (2004) Analyzing absolute paleointensity determinations:
651 Acceptance criteria and the software ThellierTool4.0. *Geochem Geophys Geosys* 5
652 doi:10.1029/2004GC000807
- 653 Leonhardt R, Soffel HC (2002) A reversal of the Earth's magnetic field recorded in mid Miocene lava
654 flows of Gran Canaria, Paleointensities. *J Geophys Res* 107:2299 doi:10.1029/2001JB000949.
- 655 Marshall M, Chauvin A, Bonhommet N (1988) Preliminary paleointensity measurements and detailed
656 magnetic analyses of basalts from the Skalamaelifell excursion, southwest Iceland. *J Geophys*
657 *Res* 93:11681-11698. doi: 10.1029/JB093iB10p11681.
- 658 Mauritsch H (1972) Paläomagnetische Messungen an west- und oststeirischen Vulkaniten. *Archiv für*
659 *Lagerstättenforschung in den Ostalpen* 13:35-57.
- 660 McDougall I, Harrison TM (1999) *Geochronology and thermochronology by the $^{40}\text{Ar}/^{39}\text{Ar}$ method.*
661 Oxford University Press, New York
- 662 Muxworthy AR (2017) Considerations for Latitudinal Time-Averaged-Field Palaeointensity Analysis of
663 the Last Five Million Years. *Front Earth Sci* 5:79. doi: 10.3389/feart.2017.00079.
- 664 Neubauer F, Genser J (1990) Architektur und Kinematik der östlichen Zentralalpen - eine Übersicht.
665 *Mitteilungen des Naturwissenschaftlichen Vereines für Steiermark* 120:203-219.
- 666 Ogg JG, Ogg GM, Gradstein FM (2016) *A Concise Geologic Time Scale: 2016.* Elsevier, Amsterdam.
- 667 Pohl J, Soffel HC (1982) Paleomagnetism of tertiary volcanics of Styria (Austria). *Geologisches Jahrbuch*
668 52:137-147.
- 669 Pöschl I (1994) A Model for the Depositional Evolution of the Volcanoclastic Succession of a Pliocene
670 Maar Volcano in the Styrian Basin (Austria). *Jahrbuch der Geologischen Bundesanstalt*
671 134:809-843.
- 672 Paterson GA, Tauxe L, Biggin AJ, Shaar R, Jonestrask LC (2014) On improving the selection of
673 Thellier-type paleointensity data. *Geochem Geophys Geosyst* 15:1180-1192
674 doi:10.1002/2013GC005135.

- 675 Paterson GA, Biggin AJ, Hodgson E, Hill MJ (2015) Thellier-type paleointensity data from multidomain
676 specimens. *Phys Earth Planet Int* 245:117-133. doi: 10.1016/j.pepi.2015.06.003.
- 677 Renne PR, Mundil R, Balco G, Min K, Ludwig KR (2010) Joint determination of ^{40}K decay constants and
678 $^{40}\text{Ar}^*/^{40}\text{K}$ for the Fish Canyon sanidine standard, and improved accuracy for $^{40}\text{Ar}/^{39}\text{Ar}$
679 geochronology. *Geochim. Cosmochim. Acta* 74:5349-5367. doi: 10.1016/j.gca.2010.06.017.
- 680 Riisager J, Riisager P, Pedersen AK (2003) The C27n-C26r geomagnetic polarity reversal recorded in the
681 west Greenland flood basalt province: How complex is the transitional field? *J Geophys Res*
682 108:B3, 2155 doi:10.1029/2002JB002124.
- 683 Singer BS (2014). A Quaternary geomagnetic instability time scale. *Quaternary Geochronology* 21:29–52.
684 doi:10.1016/j.quageo.2013.10.003.
- 685 Seghedi I, Downes H, Vaselli O, Szakács A, Balogh K, Pécskay Z (2004) Post-collisional Tertiary–
686 Quaternary mafic alkalic magmatism in the Carpathian–Pannonian region: a review.
687 *Tectonophysics* 393:43- 62. doi: 10.1016/j.tecto.2004.07.051.
- 688 Tauxe L, Shaar R, Jonestrask L, Swanson-Hysell NL, Minnett R, Koppers AAP, Constable CG, Jarboe N,
689 Gaastra K, Fairchild L (2016) PmagPy: software package for paleomagnetic data analysis and a
690 bridge to the Magnetism Information Consortium (MagIC) Database. *Geochem Geophys Geosyst*
691 17:2450-2463. doi: 10.1002/2016GC006307.
- 692 Tric E, Laj C, Valet JP, Tucholka P, Paterne M, Guichard F (1991) The Blake geomagnetic event:
693 transition geometry, dynamical characteristics and geomagnetic significance. *Earth Planet Sci*
694 *Lett* 102:1-13. doi: 10.1016/0012-821X(91)90013-8.
- 695 Valet J P, Laj C (1984) Invariant and changing transition field configurations in a sequence of
696 geomagnetic reversals. *Nature* 311:552-555. doi: 10.1038/311552a0.
- 697 Zirkl EJ, Braitsch O, Hofer F, Kahler E (1962) Neues über den Basalt von Kollnitz im Lavanttal Kärnten.
698 *Tschemaks min u petr Mitt* 8:96-139.

699

700 **Figure legends**

701 **Fig. 1:** Geological setting (modified from Gross et al. 2007) and sampling locations of
702 this study (black triangles) and of Pohl and Soffel (1982, green triangles).

703 **Fig. 2:** Representative examples of five types of bulk susceptibility thermomagnetic
704 curves. Heating is shown in red, cooling in blue, and thermal cycling in gray/black.

705 **Figure 3:** Hysteresis parameters (ratio of saturation magnetizations vs ratio of
706 coercivity) plotted in a Day-diagram (Day et al. 1977) with fields of single domain (SD),
707 pseudo single domain (PSD) multi domain (MD) grains. Black lines indicate mixtures
708 of SD and MD grains after Dunlop (2002).

709 **Fig. 4:** AF (black) and thermal (gray) demagnetization results from (a) Altenmarkt, (b)
710 Stein, (c) Stradner Kogel and (d) Waltra sites in orthogonal projections. NRM is
711 indicated by a larger symbol. North component is plotted versus East component
712 (closed symbol) and vertical component versus horizontal component (solid symbol).
713 Numbers give demagnetization steps in mT or °C. Specimen names are indicated and
714 NRM intensity is given in A/m.

715 **Fig. 5:** Demagnetizations curves from the Steinberg site. Same representation as in Fig.
716 4.

717 **Fig. 6:** Histograms of MDT (top) and MDF (bottom) for the Steinberg site (left) and the
718 Klöch site (right).

719 **Fig. 7:** Equal area projection of AF demagnetization data obtained from Klöch. Open
720 symbols represent negative inclinations, closed symbols positive. The NRM is indicated
721 by a larger symbol. Great circles fitted to the secondary component are shown in gray.
722 The gray star gives the present field direction.

723 **Fig. 8:** Demagnetizations plots for (a) Klöch quarry, (b) Zaraberg, (c) Neuhaus and (d)
724 Tieschen sites. Same representation as in Fig. 4.

725 **Fig. 9:** Examples of Thellier-Coe experiments shown in Arai plots with pTRM checks
726 as triangles, and accepted steps as dots. The insets show orthogonal vector component
727 projections in sample coordinates (vertical plane: open, blue symbols; horizontal plane:
728 solid, red symbols, green line: mean direction associated with the chosen temperature
729 interval). Further information can be found in Table S3 and Fig. S3.

730 **Fig. 10:** Mean characteristic remanent magnetizations and α_{95} of the Styrian volcanic
731 rocks. The gray area shows the expected of secular variation. Data from Pohl and Soffel
732 (1982) are shown for comparison.

733 **Fig. 11:** Mean virtual geomagnetic pole (VGP) positions obtained in this study (circle,

734 with error ellipses) in comparison with data of Pohl and Soffel (1982, green stars).

735 Three clusters were identified (see text for details).

736 **Fig. 12:** Map of the Styrian basin showing main geological units, and tectonic and

737 volcanic features (modified from Bojar et al. 2013). Paleomagnetic sites and results are

738 included.

739 **Fig. 13:** Summary of paleointensity results. Individual values and site means are plotted

740 with error bars/bands versus specimen names for the 3 VGP clusters (see Fig. 11).

741 **Fig. 14:** (a) Clusters of virtual geomagnetic poles from Styria. (b) $^{39}\text{Ar}/^{40}\text{Ar}$ -ages with 2

742 sigma errors from individual samples are shown together with their weighted mean and

743 error band in comparison with the geomagnetic instability time scale (Singer 2014, Ogg

744 et al. 2016).

745

746 **Declarations**

747 **Ethics approval and consent to participate**

748 Not applicable

- 749 **Consent for publication**
- 750 Not applicable
- 751 **List of abbreviations**
- 752 **AF:** alternating field
- 753 **ChRM:** characteristic remanent magnetization
- 754 **GPTS:** geomagnetic polarity time scale
- 755 **IRM:** isothermal remanent magnetization
- 756 **MDT:** median destructive temperature
- 757 **MDF:** median destructive field
- 758 **NRM:** natural remanent magnetization
- 759 **PCA:** principal component analysis
- 760 **VSM:** vibration sample magnetometer

761 **VGP:** virtual geomagnetic pole

762 **Availability of data and materials**

763 The directional and paleointensity data associated with this publication are available

764 from <https://github.com/PaleoInt/EPS-2021-Styria/>.

765 **Competing interests**

766 The authors declare that they have no competing interests.

767 **Funding**

768 The study was supported by Austrian science fund, grant P 30523

769 **Acknowledgements**

770 Extensive sampling was possible in the quarries of Mühldorf and Hochstraden thanks to

771 permission of Dipl.-Ing. Christian Appel (Steirische Basalt- u. Hartgesteinwerke) and in

772 Klöch quarry thanks to permission of Geschäftsführer Otto Nell (ALAS Klöch GmbH).

773 Some of the samples were cut and demagnetized in the paleomagnetic laboratory of the

774 LIAG (Grubenhagen), ES kindly acknowledges cooperation with Christian Rolf. The

775 sites of Klösch volcano were investigated by Maria Nievoll in her master thesis and
776 those of Tieschen by Julia McLaughlin in her bachelor thesis under supervision of RS.
777 Julia McLaughlin, Oliver Pöschl, Arno Ammerer and Timo Krause helped to perform
778 the paleomagnetic measurements. Thank you to Martin Gross who provided the
779 geological map of (Fig. 1).

780 **Authors' information**

781 Affiliations

782 **Palaeomagnetic Laboratory Gams, Chair of Applied Geophysics,**

783 **Montanuniversität Leoben, Gams 45, A8130 Frohnleiten, Austria**

784 Elisabeth Schnepf, Robert Scholger

785 **Conrad Observatorium, ZAMG - Zentralanstalt für Meteorologie und**

786 **Geodynamik, Hohe Warte 38, 1190 Vienna, Austria**

787 Patrick Arneitz, Ramon Egli, Roman Leonhardt

788 **Geological Survey of Norway, P.O. Box 6315 Torgarden, NO-7491 Trondheim,**

789 **Norway**

790 Morgan Ganerød

791 **Universalmuseum Joanneum, Studienzentrum Naturkunde, Weinzöttlstraße 16,**

792 **8045 Graz, Austria**

793 Ingomar Fritz

794 **Authors' contributions**

795 Field work was done by ES, PA, IF, RS and RL. Paleo and rock magnetic results were

796 produced by ES, PA, RS and RE. Dating was performed by MG. ES wrote the paper

797 with contributions of PA, IF, MG and RS. All authors read and approved the final

798 manuscript.

799 **Corresponding author**

800 Correspondence to Elisabeth Schnepf

801 **Appendix**

802 **Supplementary figures:**

803 **Figure S1:** $\kappa(T)$ -curves (left) and thermal cycling (right). The $\kappa(T)$ -curve type is given
804 (see text). One representative example for each type from each site (cf. Table-1 and S3)
805 is shown.

806 [Supplementary_Figure_S1.pdf](#)

807 **Figure S2:** Directions of ChRM (black) are plotted together with the mean ChRM (red)
808 and its 95% confidence circle for each site (cf. Table-1) in equal area stereographic net.
809 Open symbols indicate reversed and closed symbols normal directions. Green stars are
810 the mean ChRMs obtained by Pohl and Soffel (1982) from the same rock unit.

811 [Supplementary_Figure_S2.pdf](#)

812 **Figure S3:** Additional information of paleointensity experiments of Fig.-Arai. NRM
813 decay curve (left) with results of the tail checks, and plots of angular difference of
814 HL-pTRM (upper middle), δ CK is the relative check error normalized to the TRM
815 (lower middle), δ t* is the normalized tail of pTRM corrected for the angular difference
816 between the applied field and the NRM (upper right) and δ TR is the difference between
817 first and repeated demagnetization (lower right).

818 [Supplementary_Figure_S3.pdf](#)

819 **Figure S4:** $^{39}\text{Ar}/^{40}\text{Ar}$ - incremental heating experiments with degassing spectra (left) and
820 inverse isochron plots (right). a) to d) samples from Klöch volcano and e) to j) samples
821 from Steinberg volcano.

822 [Supplementary_Figure_S4.pdf](#)

823

824 **Additional files**

825 **Table S1:** Paleointensity results on specimen level in [Supplementary_table_S1.xlsx](#)

826 **Table S2:** Raw data of $^{39}\text{Ar}/^{40}\text{Ar}$ - incremental heating experiments in

827 [Supplementary_table_S2.xlsx](#)

828 **Table S3:** Results of $\kappa(T)$ -curves in Supplementary_table_S3.xlsx

829 **Table S4:** Results of hysteresis measurements in Supplementary_table_S4.xlsx

830 Description of data are given within the files.

Figures

Fig. 1

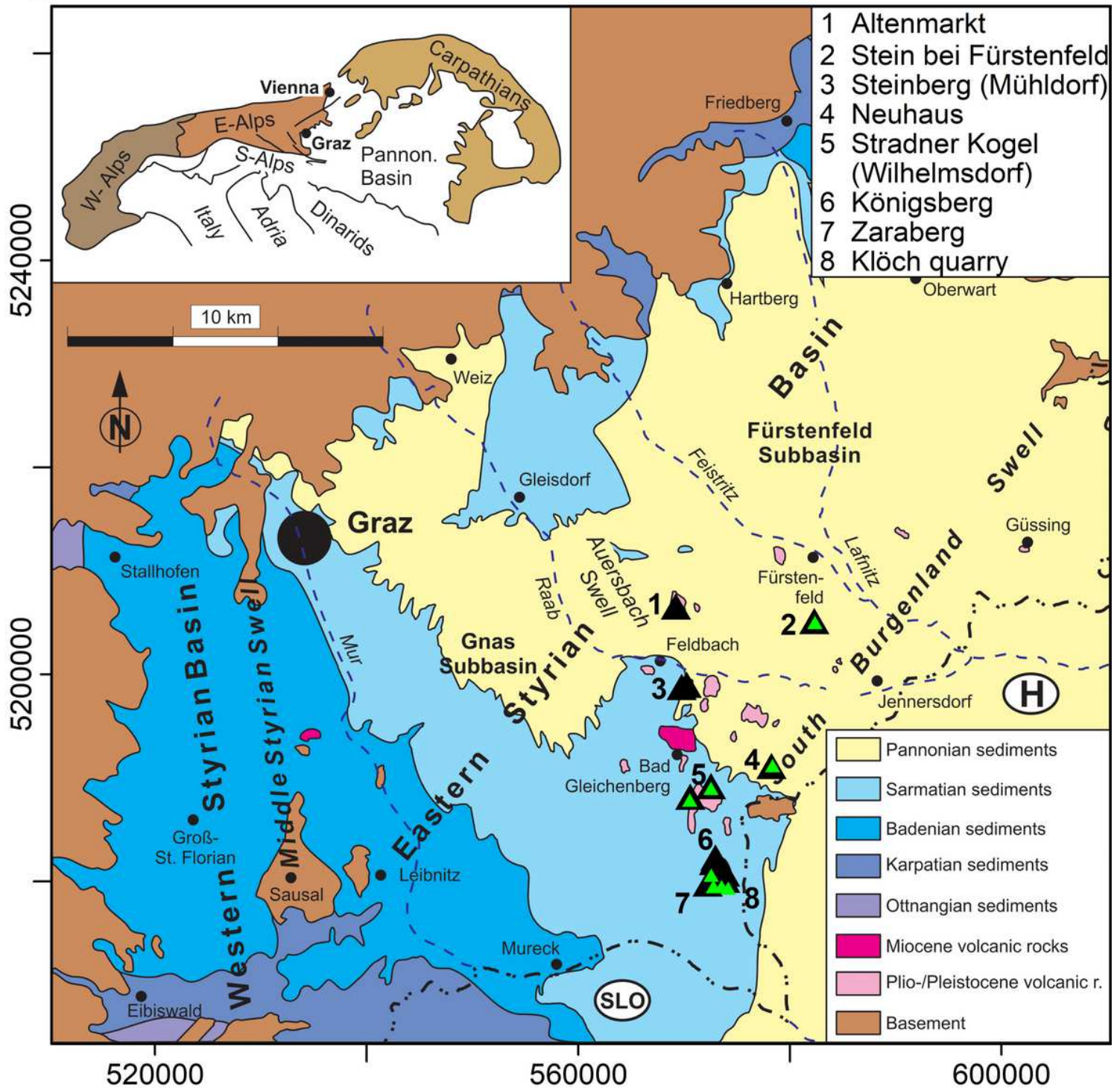


Figure 1

Geological setting (modified from Gross et al. 2007) and sampling locations of this study (black triangles) and of Pohl and Soffel (1982, green triangles). Note: The designations employed and the presentation of the material on this map do not imply the expression of any opinion whatsoever on the

part of Research Square concerning the legal status of any country, territory, city or area or of its authorities, or concerning the delimitation of its frontiers or boundaries. This map has been provided by the authors.

Fig. 2

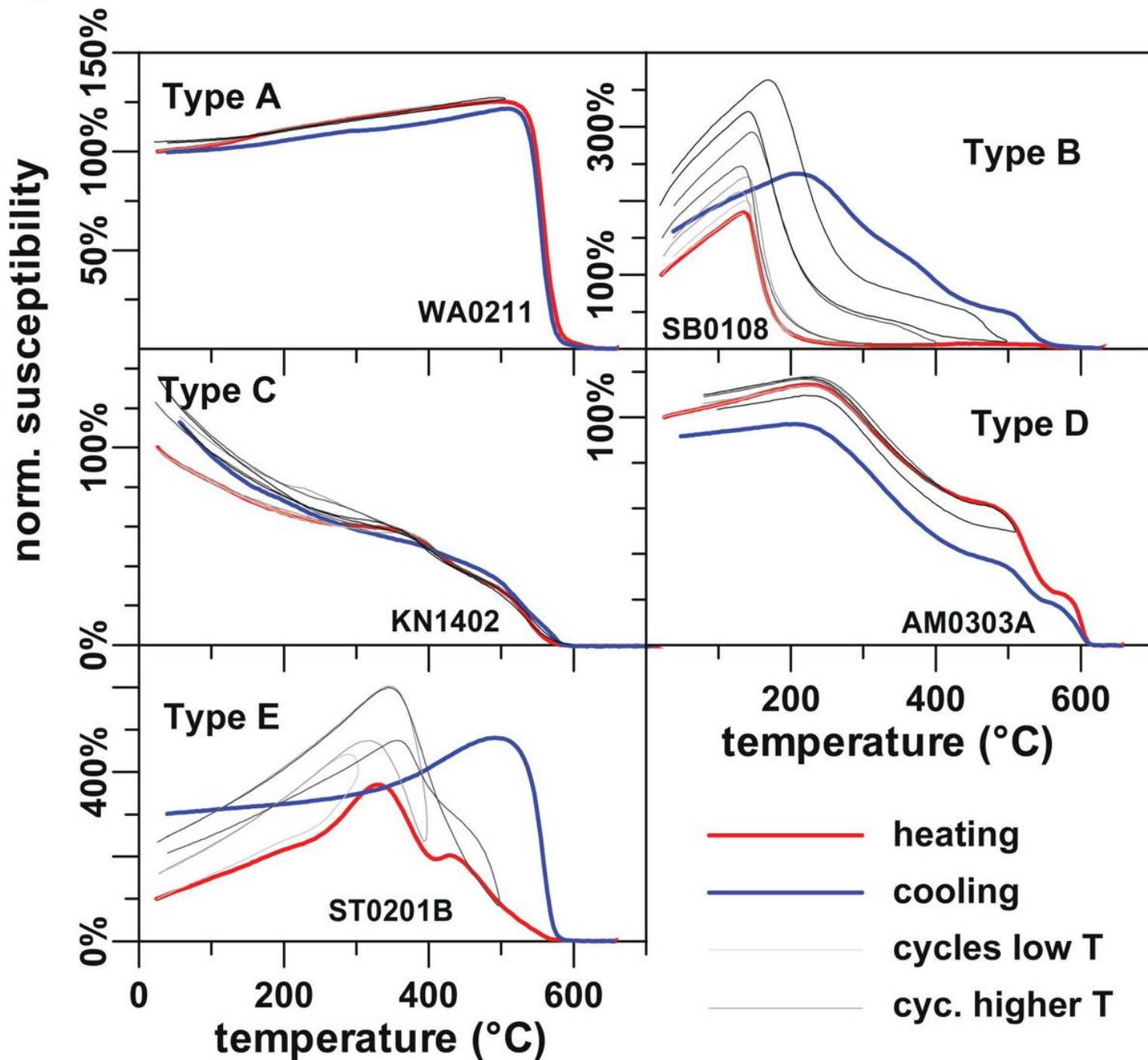


Figure 2

Representative examples of five types of bulk susceptibility thermomagnetic curves. Heating is shown in red, cooling in blue, and thermal cycling in gray/black.

Fig. 3

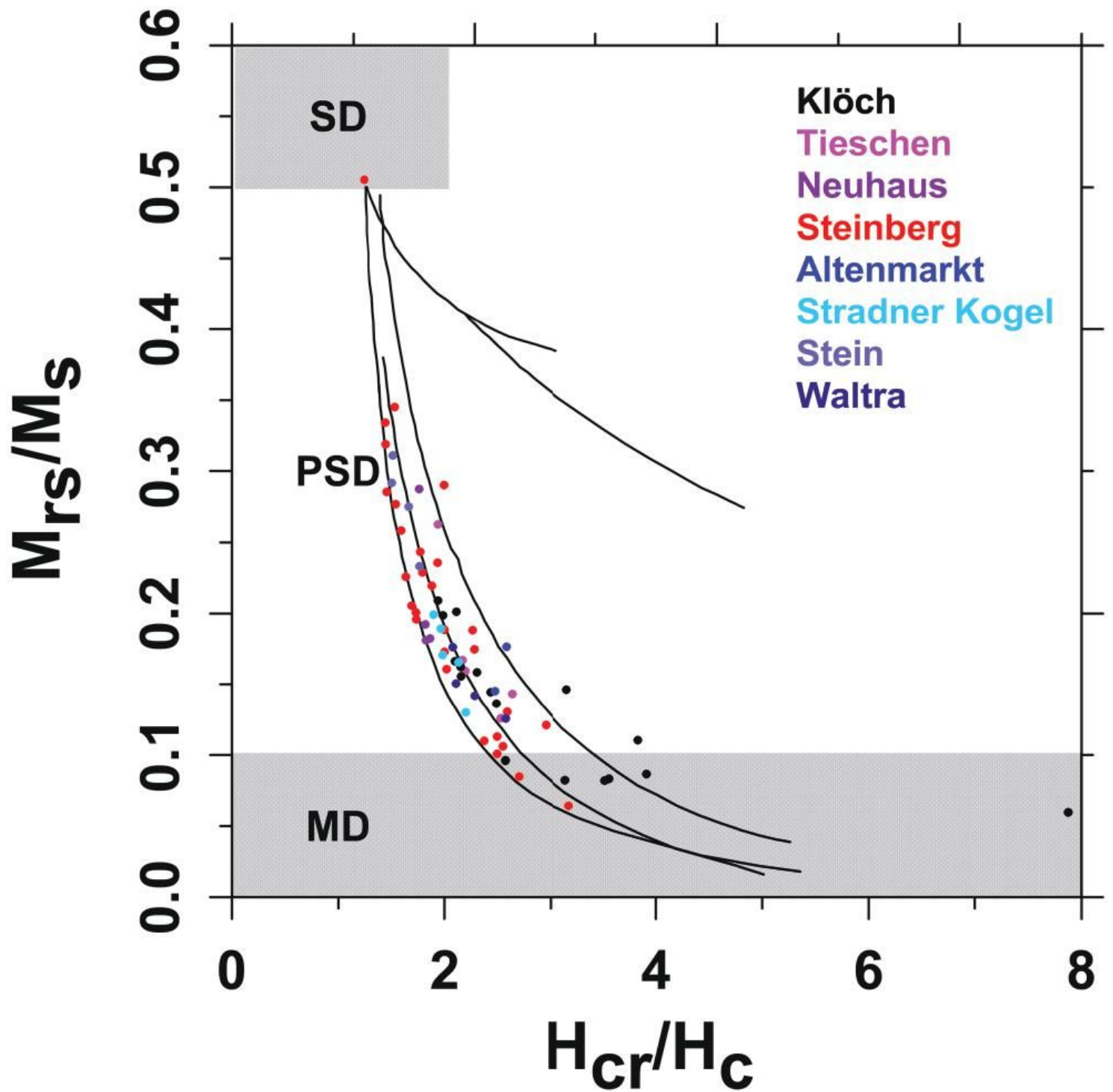


Figure 3

Hysteresis parameters (ratio of saturation magnetizations vs ratio of coercivity) plotted in a Day-diagram (Day et al. 1977) with fields of single domain (SD), pseudo single domain (PSD) multi domain (MD) grains. Black lines indicate mixtures of SD and MD grains after Dunlop (2002).

Fig. 4

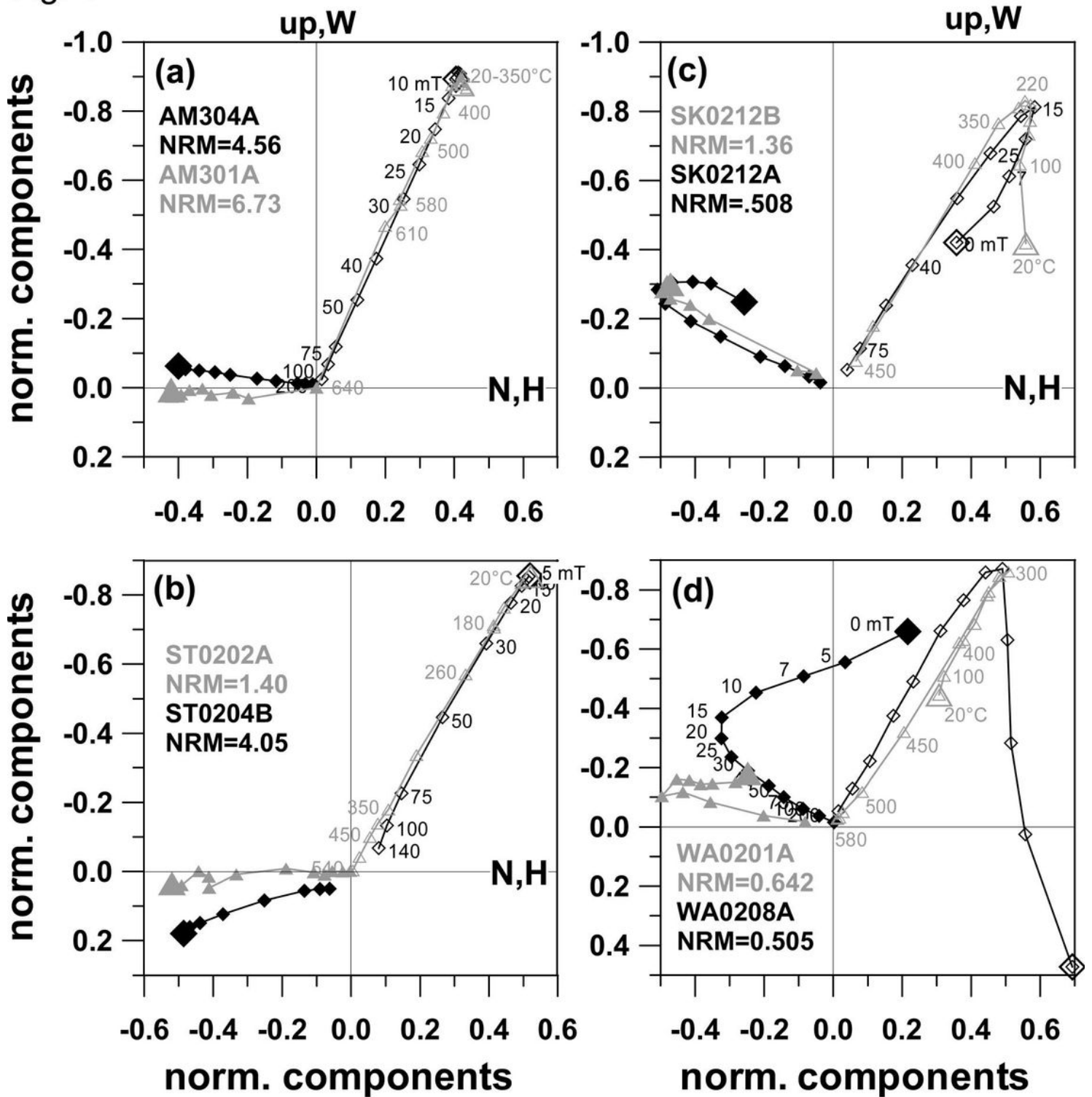


Figure 4

AF (black) and thermal (gray) demagnetization results from (a) Altenmarkt, (b) Stein, (c) Stradner Kogel and (d) Waltra sites in orthogonal projections. NRM is indicated by a larger symbol. North component is plotted versus East component (closed symbol) and vertical component versus horizontal component (solid symbol). Numbers give demagnetization steps in mT or °C. Specimen names are indicated and NRM intensity is given in A/m.

Fig. 5

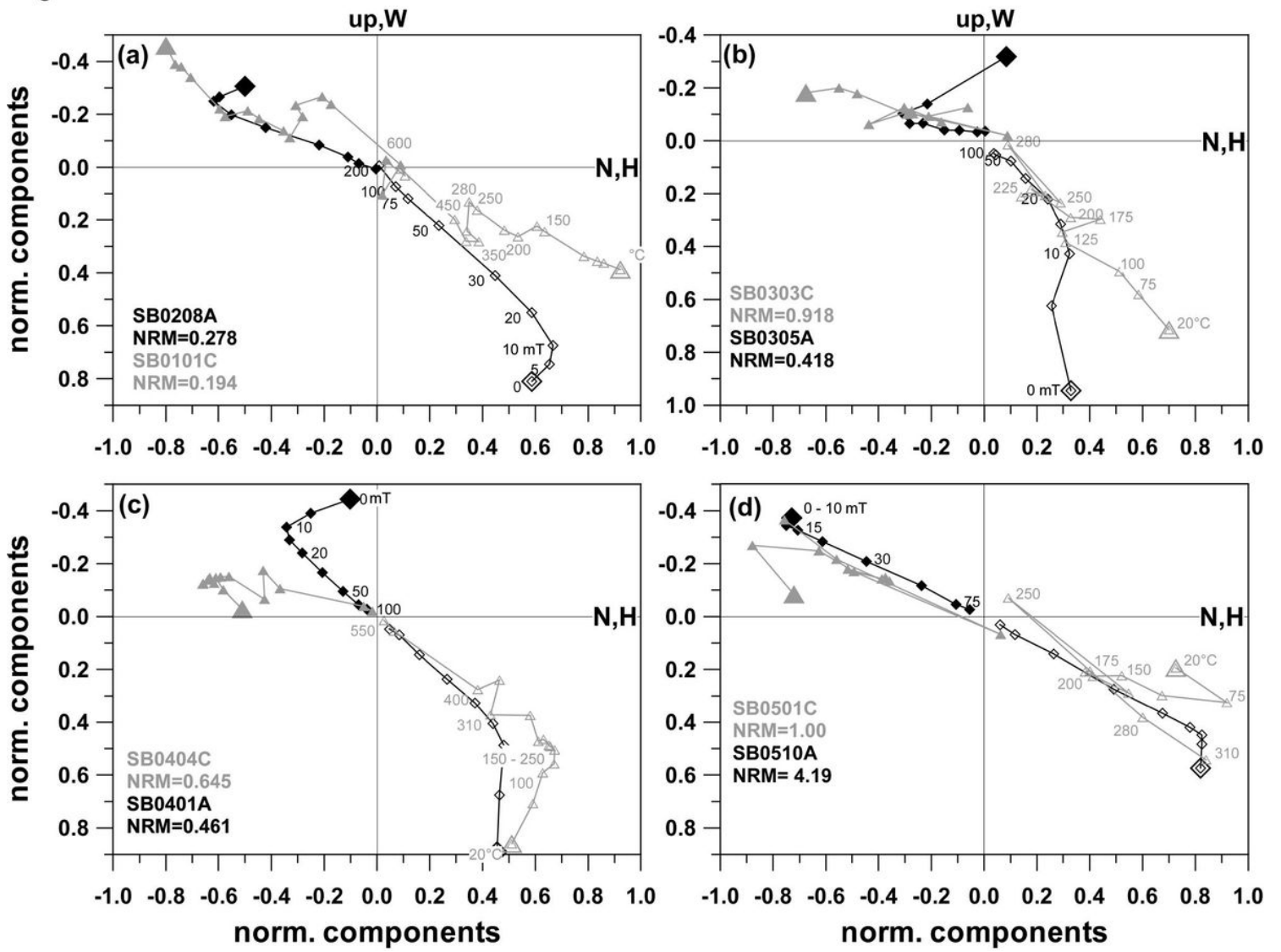


Figure 5

Demagnetizations curves from the Steinberg site. Same representation as in Fig. 4.

Fig. 6

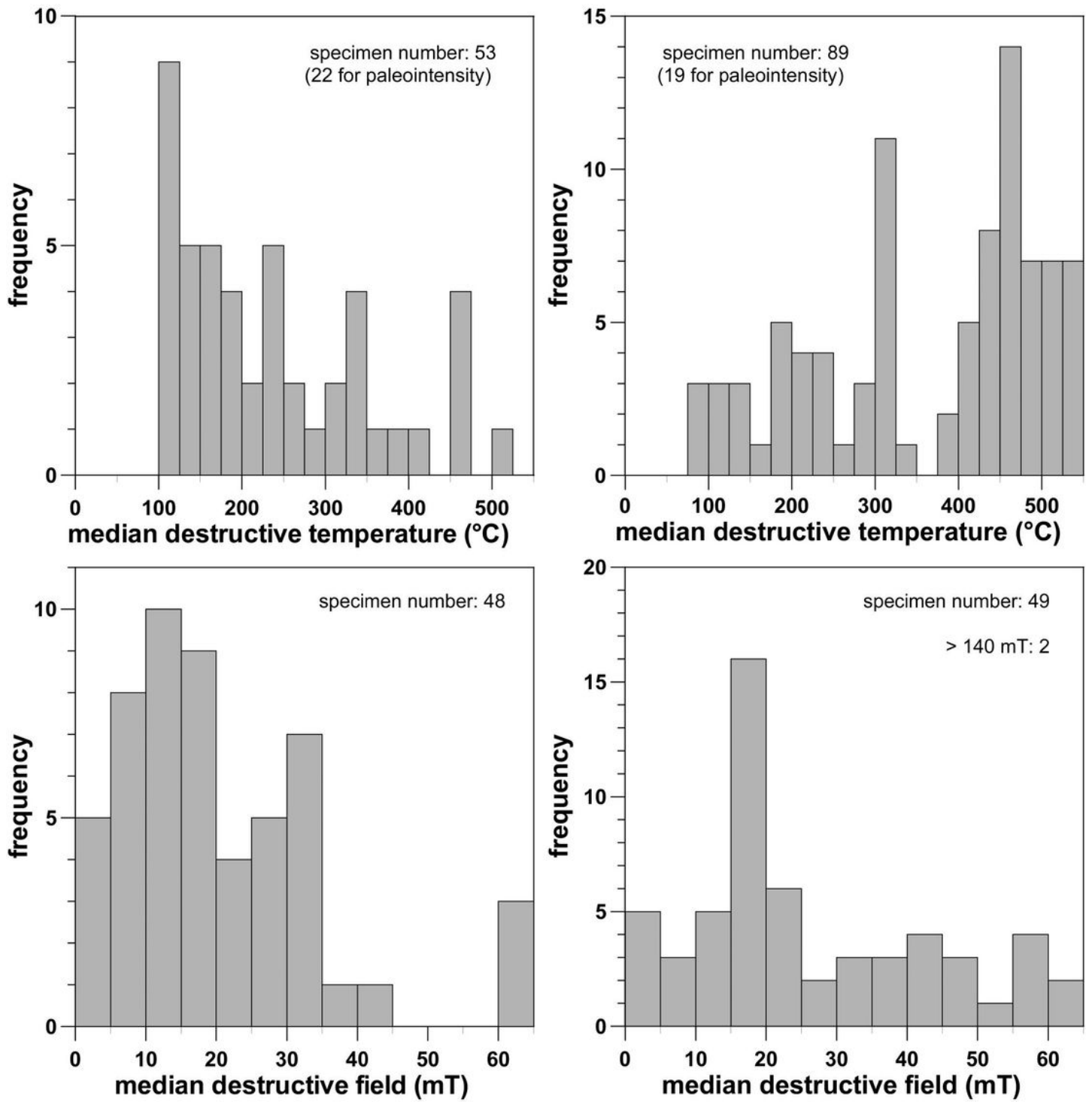


Figure 6

Histograms of MDT (top) and MDF (bottom) for the Steinberg site (left) and the Klöch site (right).

Fig. 7

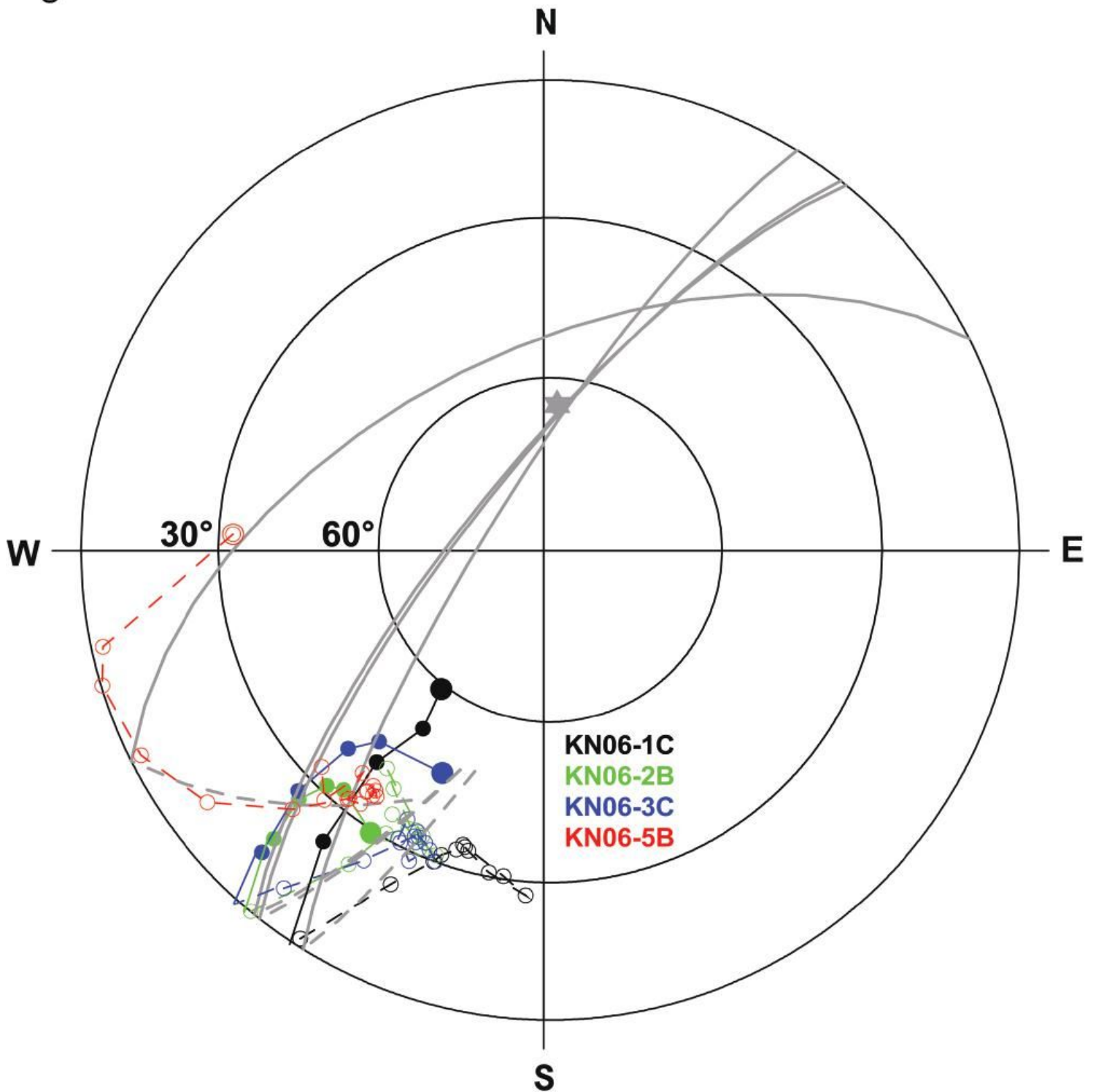


Figure 7

Equal area projection of AF demagnetization data obtained from Klösch. Open symbols represent negative inclinations, closed symbols positive. The NRM is indicated by a larger symbol. Great circles fitted to the secondary component are shown in gray. The gray star gives the present field direction.

Fig. 8

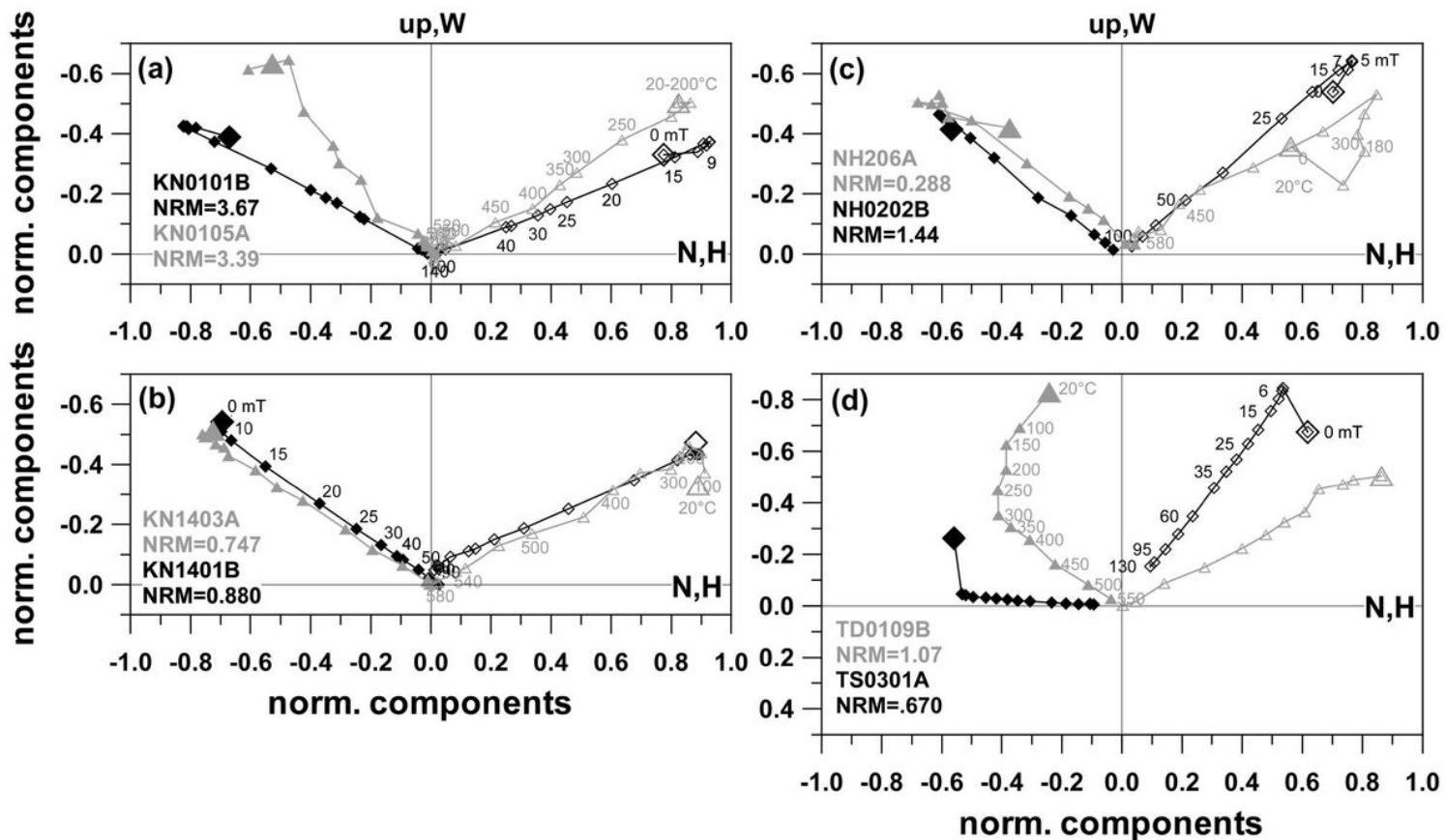


Figure 8

Demagnetizations plots for (a) Klösch quarry, (b) Zaraberg, (c) Neuhaus and (d) Tieschen sites. Same representation as in Fig. 4.

Fig. 9

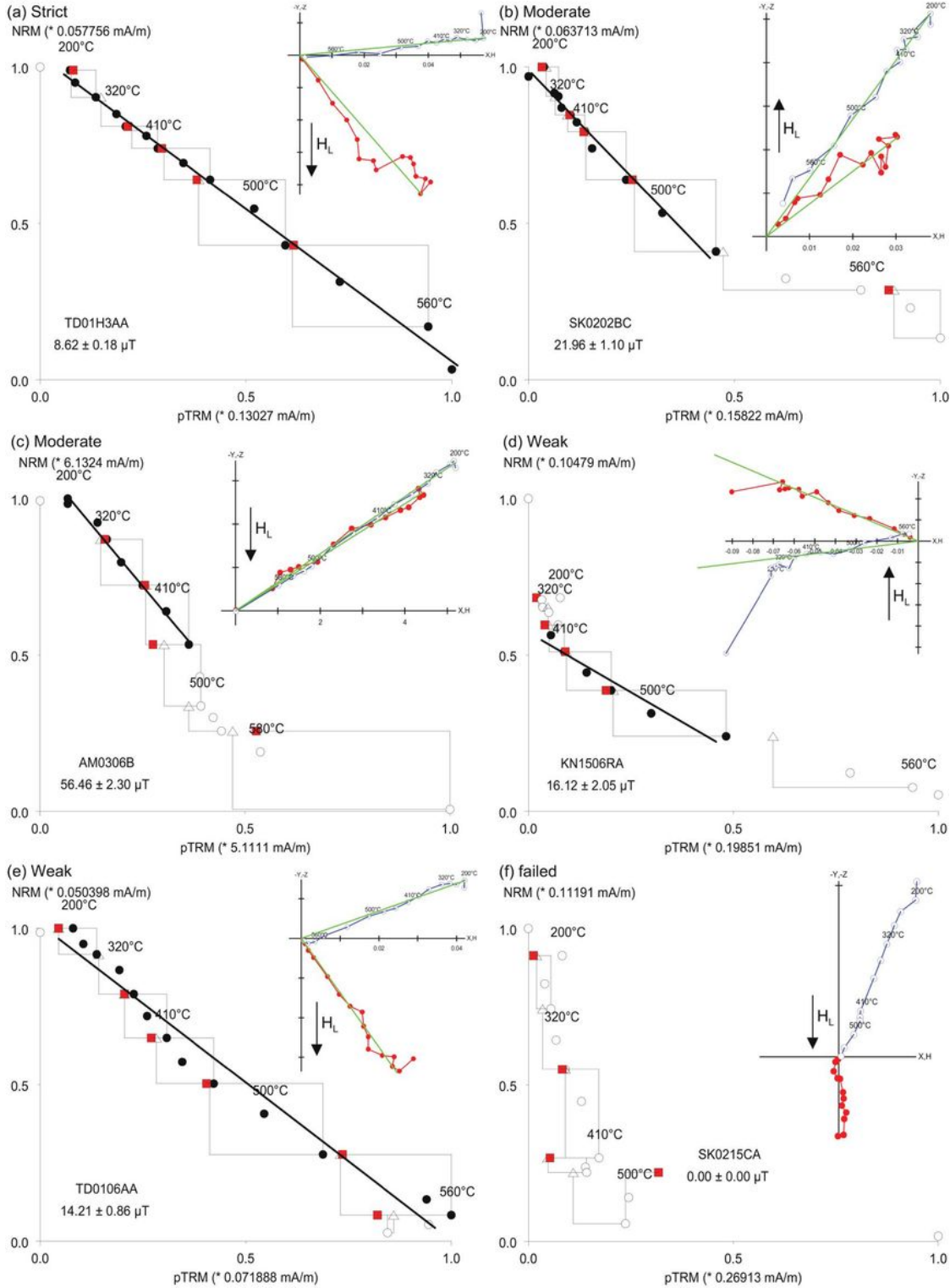


Figure 9

Examples of Thellier-Coe experiments shown in Arai plots with pTRM checks as triangles, and accepted steps as dots. The insets show orthogonal vector component projections in sample coordinates (vertical plane: open, blue symbols; horizontal plane: solid, red symbols, green line: mean direction associated with the chosen temperature interval). Further information can be found in Table S3 and Fig. S3.

Fig. 10

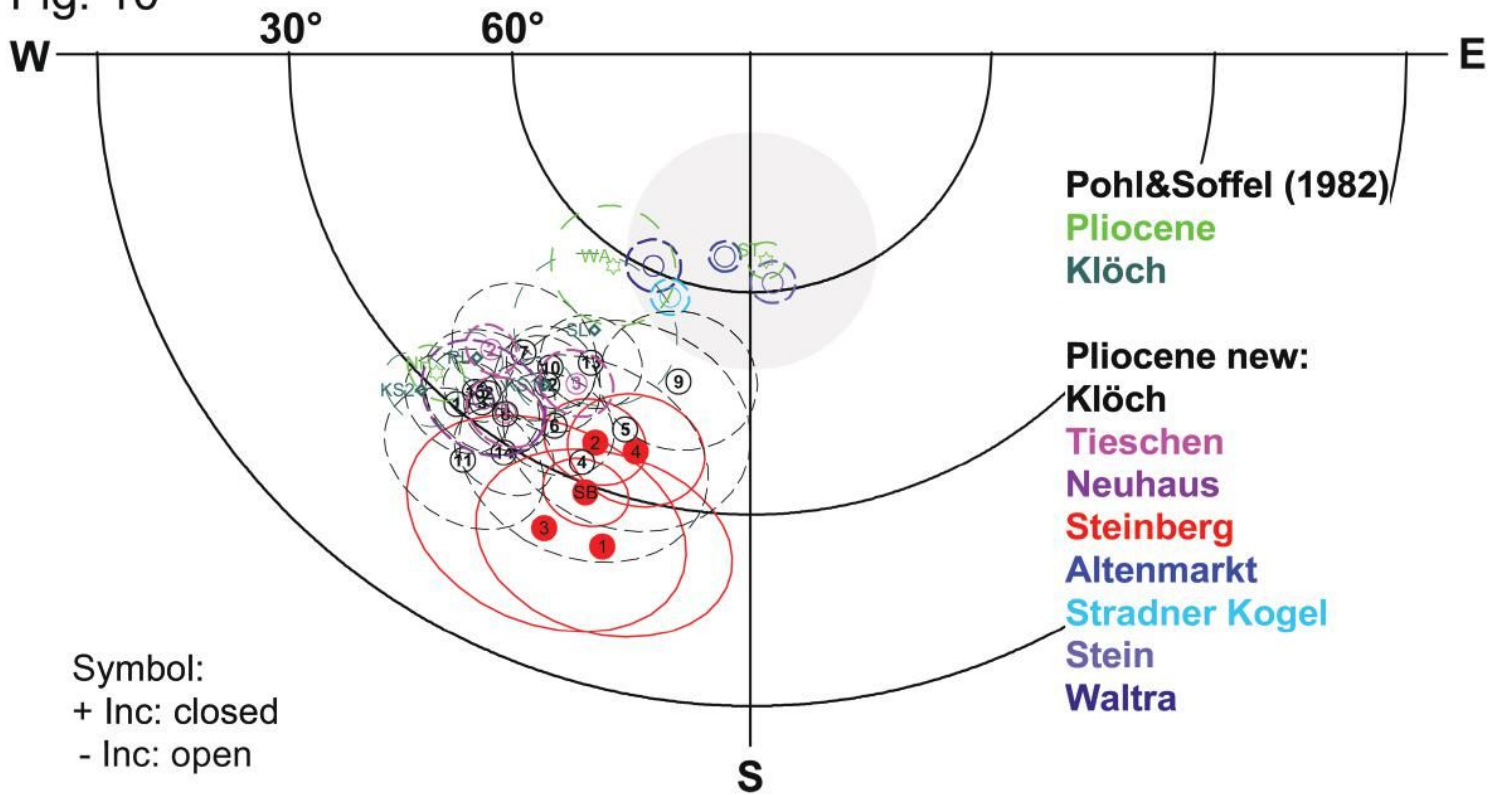


Figure 10

Mean characteristic remanent magnetizations and α_{95} of the Styrian volcanic rocks. The gray area shows the expected of secular variation. Data from Pohl and Soffel (1982) are shown for comparison.

Fig. 11

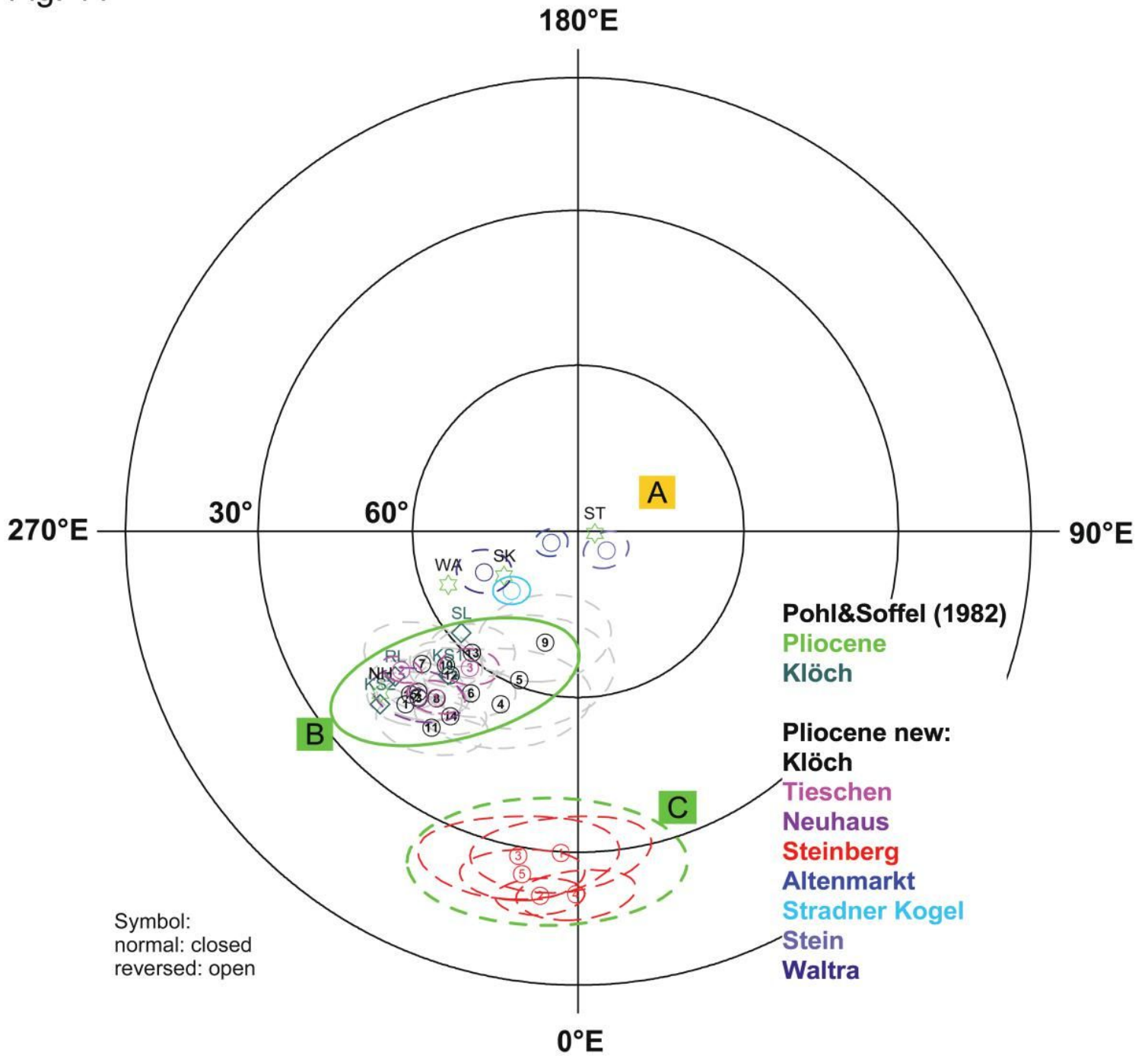


Figure 11

Mean virtual geomagnetic pole (VGP) positions obtained in this study (circle, with error ellipses) in comparison with data of Pohl and Soffel (1982, green stars). Three clusters were identified (see text for details).

Fig. 12

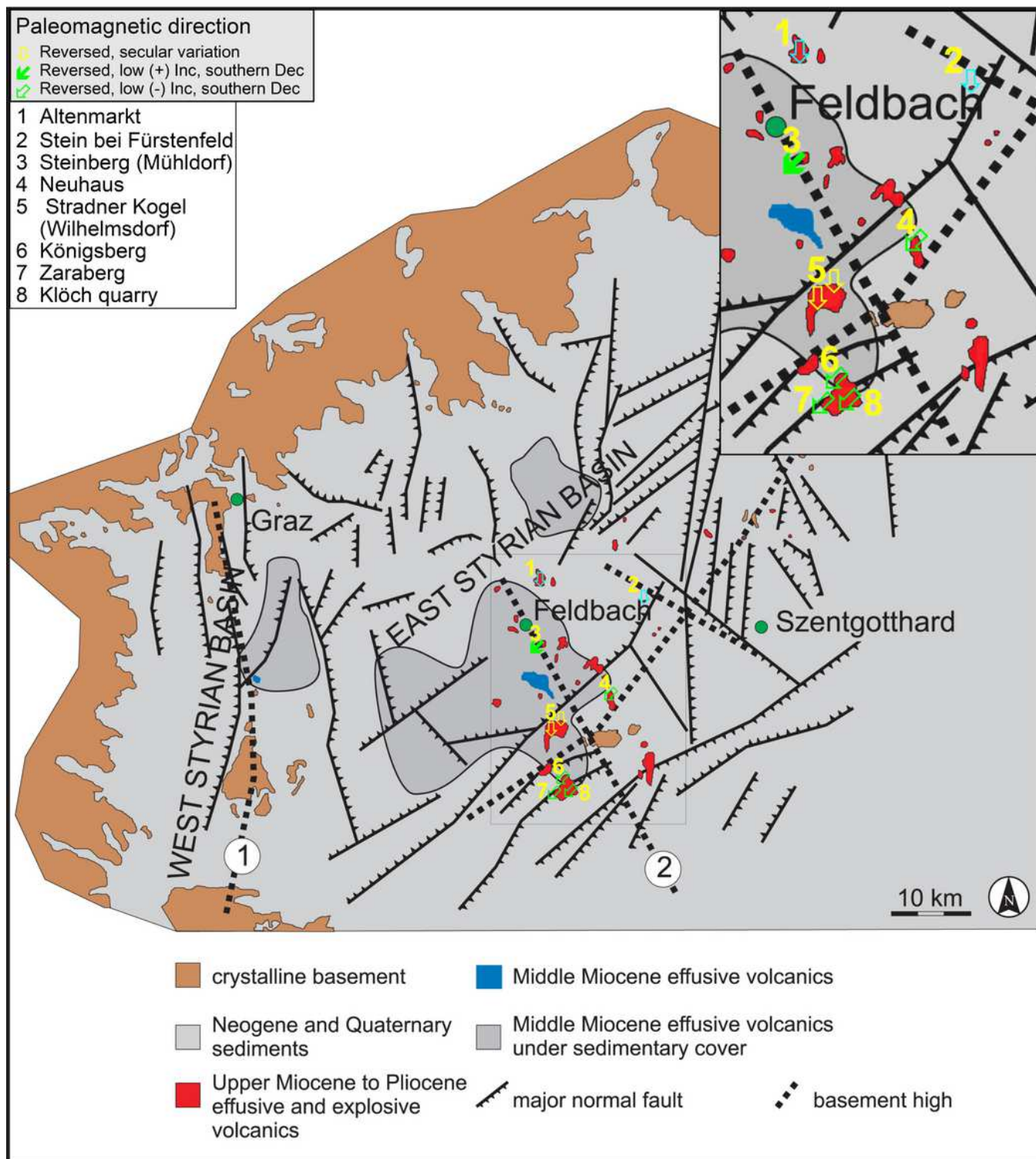


Figure 12

Map of the Styrian basin showing main geological units, and tectonic and volcanic features (modified from Bojar et al. 2013). Paleomagnetic sites and results are included. Note: The designations employed and the presentation of the material on this map do not imply the expression of any opinion whatsoever on the part of Research Square concerning the legal status of any country, territory, city or area or of its

authorities, or concerning the delimitation of its frontiers or boundaries. This map has been provided by the authors.

Fig. 13

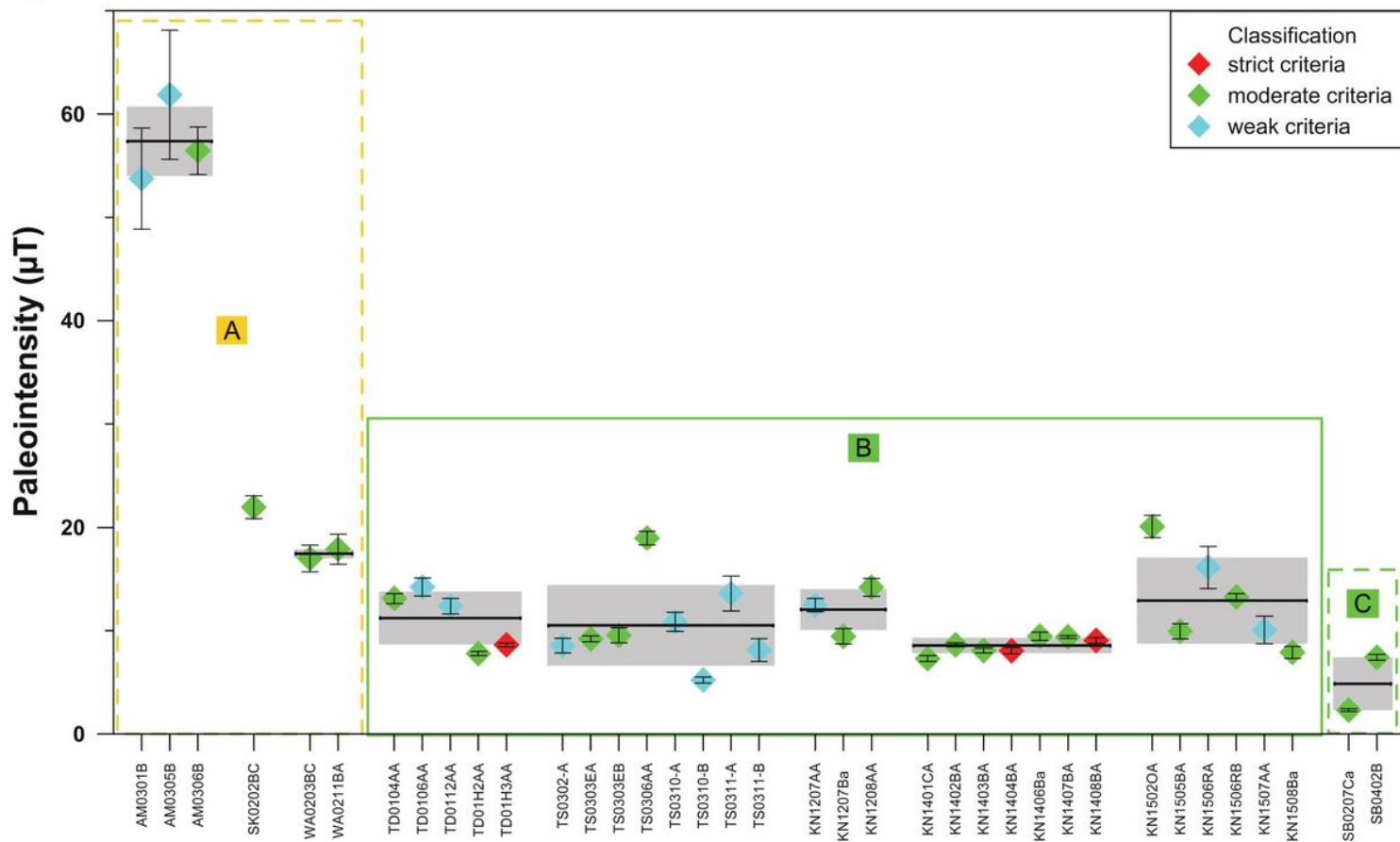


Figure 13

Summary of paleointensity results. Individual values and site means are plotted with error bars/bands versus specimen names for the 3 VGP clusters (see Fig. 11).

Fig. 14

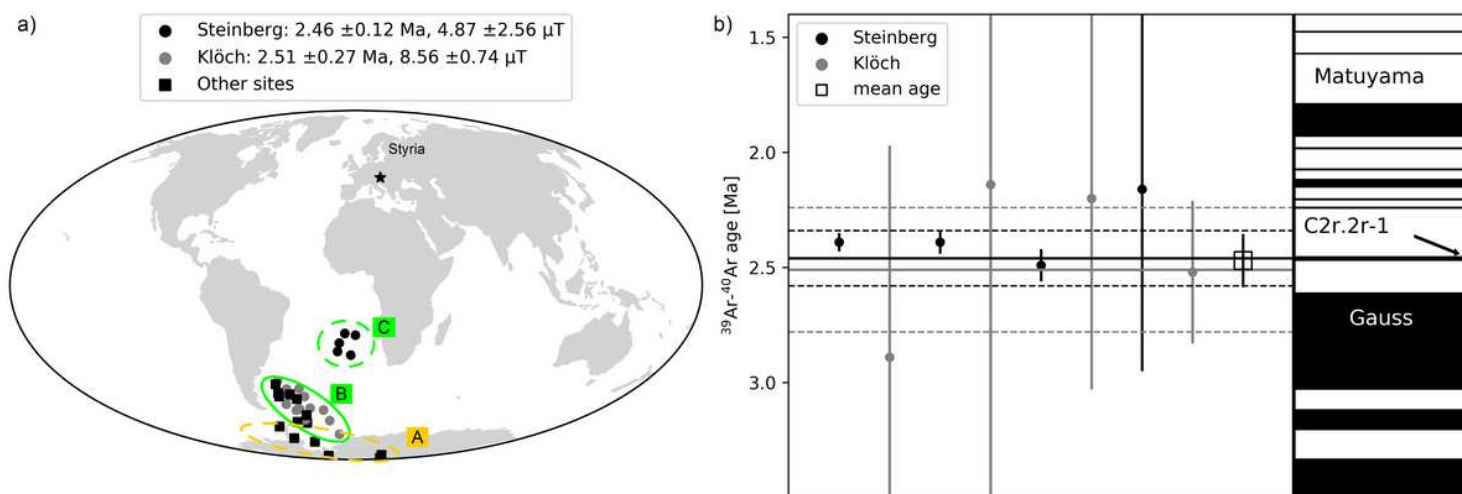


Figure 14

(a) Clusters of virtual geomagnetic poles from Styria. (b) $^{39}\text{Ar}/^{40}\text{Ar}$ -ages with 2 sigma errors from individual samples are shown together with their weighted mean and error band in comparison with the geomagnetic instability time scale (Singer 2014, Ogg et al. 2016). Note: The designations employed and the presentation of the material on this map do not imply the expression of any opinion whatsoever on the part of Research Square concerning the legal status of any country, territory, city or area or of its authorities, or concerning the delimitation of its frontiers or boundaries. This map has been provided by the authors.

Supplementary Files

This is a list of supplementary files associated with this preprint. Click to download.

- [SupplementaryFigureS1.pdf](#)
- [GraphicalAbstractImage.png](#)
- [SupplementarytableS1.xlsx](#)
- [SupplementarytableS2.xlsx](#)
- [SupplementarytableS3.xlsx](#)
- [SupplementarytableS4.xlsx](#)
- [SupplementaryFigureS2.pdf](#)
- [SupplementaryFigureS3.pdf](#)
- [SupplementaryFigureS4.pdf](#)